The Astrophysical Journal, 973:16 (27pp), 2024 September 20 https://doi.org/10.3847/1538-4357/ad675a
© 2024. The Author(s). Published by the American Astronomical Society.
OPEN ACCESS

# Suppressed Cosmic-Ray Energy Densities in Molecular Clouds from Streaming Instability-regulated Transport

Margot Fitz Axen[1], Stella Offner[1], Philip F. Hopkins[2], Mark R. Krumholz[3,4], and Michael Y. Grudić[5]
[1] Department of Astronomy, The University of Texas at Austin, 2515 Speedway, Stop C1400, Austin, TX 78712-1205, USA; fitza003@utexas.edu
[2] TAPIR, Mailcode 350-17, California Institute of Technology, Pasadena, CA 91125, USA
[3] Research School of Astronomy and Astrophysics, Australian National University, Canberra ACT 2600, Australia
[4] ARC Center of Excellence for Astronomy in Three Dimensions (ASTRO-3D), Canberra ACT 2600, Australia
[5] Carnegie Observatories, 813 Santa Barbara St, Pasadena, CA 91101, USA
*Received 2024 January 12; revised 2024 July 23; accepted 2024 July 23; published 2024 September 12*

## Abstract

Cosmic rays (CRs) are the primary driver of ionization in star-forming molecular clouds (MCs). Despite their potential impacts on gas dynamics and chemistry, no simulations of star cluster formation following the creation of individual stars have included explicit cosmic-ray transport (CRT) to date. We conduct the first numerical simulations following the collapse of a $2000M_{\odot}$ MC and the subsequent star formation including CRT using the STAR FORmation in Gaseous Environments framework implemented in the GIZMO code. We show that when CRT is streaming-dominated, the CR energy in the cloud is strongly attenuated due to energy losses from the streaming instability. Consequently, in a Milky Way–like environment the median CR ionization rate in the cloud is low ($\zeta \lesssim 2 \times 10^{-19}\,\mathrm{s}^{-1}$) during the main star-forming epoch of the calculation and the impact of CRs on the star formation in the cloud is limited. However, in high-CR environments, the CR distribution in the cloud is elevated ($\zeta \lesssim 6 \times 10^{-18}$), and the relatively higher CR pressure outside the cloud causes slightly earlier cloud collapse and increases the star formation efficiency by 50% to ∼13%. The initial mass function is similar in all cases except with possible variations in a high-CR environment. Further studies are needed to explain the range of ionization rates observed in MCs and explore star formation in extreme CR environments.

*Unified Astronomy Thesaurus concepts:* Cosmic rays (329); Star formation (1569); Initial mass function (796); Ionization (2068); High energy astrophysics (739)

## 1. Introduction

Cosmic rays (CRs) are ubiquitous and responsible for driving a variety of astrochemical and dynamic processes. In the interstellar medium (ISM), CRs have an energy density of $\sim 1\,\mathrm{eV\,cm}^{-3}$, which is comparable to the energy densities of the cosmic microwave background, starlight, and galactic magnetic field (Ferrière 2001). In the densest regions of molecular clouds (MCs), which are optically thick to UV radiation, CRs are the primary driver of ionization (Dalgarno 2006). The level of CR ionization is usually quantified by the CR primary ionization rate (CRIR), which is the rate of CR ionizations per hydrogen atom per unit time.

The CRIR in the Solar neighborhood inferred from the CR particle flux measured outside the heliosphere by Voyager is $\zeta \approx 1.6 \times 10^{-17}\,\mathrm{s}^{-1}$ (Cummings et al. 2016; Stone et al. 2019). Since CR ionizations lead to chemical reactions that produce molecules such as $OH^+$, $H_2O^+$, and $H_3O^+$, measurements of these molecules can also be used to constrain the CRIR indirectly, since their abundances are sensitive to it (Indriolo et al. 2015). Observations of these molecules along different sight lines predict a range of values for the CRIR. In the Milky Way, the CRIR varies between $\approx 10^{-17}$ and $10^{-15}\,\mathrm{s}^{-1}$, with values ≈10 times higher in the Galactic center than in the Galactic disk (Indriolo et al. 2015; Neufeld & Wolfire 2017). In higher-density regions such as high-mass star-forming regions (Sabatini et al. 2020) and low-mass dense cores (Caselli et al. 1998; Bialy et al. 2022), the CRIR is expected to be lower due to attenuation by the dense gas. In contrast, recent observations near supernova (SN) remnants (SNRs; Ceccarelli et al. 2011) and toward the more active star-forming regions in the center of our Galaxy (Rivilla et al. 2022) and NGC 253 (Behrens et al. 2022; Holdship et al. 2022) suggest orders-of magnitude higher CRIRs than would be predicted from Voyager data (see review by Padovani 2023).

Some of the observed variations in the CRIR can be explained by the presence of non-SN CR acceleration sources (Ceccarelli et al. 2011). While SNRs have long been thought to be the primary source of galactic CRs (Blasi 2013), converting about 10% of their energy into CR acceleration (Vink 2012), evidence indicates that stellar winds from massive stars also accelerate CRs (Parizot et al. 2004; Bykov et al. 2020). A number of star clusters exhibit $\gamma$-ray emission, indicative of the presence of locally accelerated high-energy CRs (Ackermann et al. 2011; Yang & Aharonian 2017; Yang et al. 2018; Aharonian et al. 2019; Sun et al. 2020; Liu et al. 2022; Pandey et al. 2024). Some estimates suggest that stellar winds convert up to ∼10% of their energy into CR acceleration (Aharonian et al. 2019), while others claim it may be as high as 40% (Pandey et al. 2024). Most recently, ionization maps of star-forming regions hint that protostellar sources may also accelerate CRs (Ceccarelli et al. 2014; Cabedo et al. 2023; Pineda et al. 2024), likely accelerated by the accretion or protostellar jet shocks (Padovani et al. 2016; Gaches & Offner 2018).

Observations of CRIR variation have motivated a variety of theoretical studies on the impact of CR physics on galactic processes. To date, a growing number of hydrodynamic

Original content from this work may be used under the terms of the Creative Commons Attribution 4.0 licence. Any further distribution of this work must maintain attribution to the author(s) and the title of the work, journal citation and DOI.

simulations have included explicit cosmic-ray transport (CRT) to study the effect of CRs on galaxy formation and evolution. These calculations suggest that CR pressure may dominate over thermal pressure in the haloes of low redshift Milky Way mass galaxies, driving galactic outflows and suppressing star formation (Jubelgas et al. 2008; Uhlig et al. 2012; Booth et al. 2013; Hanasz et al. 2013; Salem et al. 2014; Pakmor et al. 2016; Simpson et al. 2016; Wiener et al. 2017; Butsky & Quinn 2018; Jacob et al. 2018; Chan et al. 2019; Dashyan & Dubois 2020; Hopkins et al. 2020; Ji et al. 2020; Farcy et al. 2022; Girichidis et al. 2022, 2024; Thomas et al. 2023). Stratified box calculations of patches of a Milky Way–like disk that include CRT indicate that including plasma-dependent transport parameters changes the impact of the CRs on the gas structure (Girichidis et al. 2016; Simpson et al. 2016; Farber et al. 2018; Holguin et al. 2019). However, all of these effects strongly depend on the prescription adopted for CRT; for example, Commerçon et al. (2019) find that when CRT is treated as purely diffusive, for diffusivities $D \lesssim 10^{25}\,\mathrm{cm^2\,s^{-1}}$ CRs are trapped in the gas by pressure gradients that modify the gas flow. This effect is particularly relevant near CR acceleration sources where the CR diffusivity is suppressed due to turbulence, causing the gas to fragment rather than group into star-forming clumps (Semenov et al. 2021). By contrast, higher diffusivities produce much smaller dynamical effects, because CRs are less effectively trapped and thus large CR pressures do not build up.

Despite evidence from observations and simulations that CR properties vary with the environment and change gas properties, most simulations and analytical models of MCs to date have neglected the impact of CRs altogether (e.g., Hennebelle & Chabrier 2008; Padoan & Nordlund 2011; Hopkins 2012; Li et al. 2015; Lee et al. 2019). Most simulations have assumed a spatially and temporally uniform CRIR of $\approx 10^{-17}$–$10^{-16}\,\mathrm{s^{-1}}$ to calculate the heating and cooling processes (Glover & Clark 2012; Bate & Keto 2015; Gatto et al. 2017; Smith et al. 2020; Grudić et al. 2021; Guszejnov et al. 2021, 2022) or have neglected CR ionization altogether. However, in addition to neglecting the impact of CRIR variation on the gas temperature, these simulations do not take into account the possible dynamical effect of CRs on the gas. For example, the level of ionization determines how much the gas couples to the magnetic field and resists collapse (Fiedler & Mouschovias 1993; Padovani et al. 2014). Simulations of protostellar collapse show that the CRIR also determines whether a protostellar disk forms and regulates its size (Wurster et al. 2018; Kuffmeier et al. 2020). CR energy deposition may also modify the gas turbulence if the CR pressure is high enough (Commerçon et al. 2019). Although some studies have investigated the effects of including CRT in MCs via post-processing, these also neglect the dynamical effects between the CRs and the gas (Fatuzzo & Adams 2014; Fitz Axen et al. 2021).

No simulations to date have both included CRT and resolved the formation of individual stars. In this study, we carry out large-scale simulations of MC collapse that include CRT in order to follow the propagation of CRs from the galactic CR background. We use the STAR FORmation in Gaseous Environments (STARFORGE) framework, which is built on the GIZMO simulation code (Hopkins 2015) and includes all relevant feedback processes, including protostellar jets, radiative heating, stellar winds, and supernovae. The fiducial STARFORGE MC simulations resolve mass scales down to $\approx 0.1 M_\odot$ and so are able to self-consistently predict the stellar initial mass function (IMF; Grudić et al. 2021, 2022; Guszejnov et al. 2021, 2022). In this work we carry out STARFORGE simulations including the GIZMO single-bin CRT treatment, which has been used extensively in the Feedback in Realistic Environments (FIRE) suite of cosmological simulations (Chan et al. 2019; Hopkins et al. 2020, 2021a, 2021b, 2021c, 2022a). This implementation applied to galaxy-scale calculations is able to reproduce observables such as the CR intensity spectrum observed by Voyager (Hopkins et al. 2021a).

In this work, we explore the impact of CRs on ionization, gas temperatures, star formation histories, and the IMF of star-forming MCs. Section 2 describes the physics and numerical methods used in the STARFORGE simulations, the GIZMO CRT modules, and the simulation initial conditions. Section 3 presents the results of simulations with different recipes for CRT. Section 4 discusses how CRT properties shape our results and compares them to prior work. Finally, Section 5 summarizes our results.

## 2. Methods

### 2.1. The STARFORGE Simulations

#### 2.1.1. Physics

We simulate star-forming MCs using the STARFORGE framework, which uses the GIZMO simulation code (Hopkins 2015). A full description of the STARFORGE methods is included in Grudić et al. (2021); therefore, we only summarize the key points here.

We use the Lagrangian constrained-gradient meshless finite-mass method for magnetohydrodynamics (MHD; Hopkins 2016; Hopkins & Raives 2016) and assume the ideal MHD limit. The simulations utilize the updated FIRE-3 radiation and chemistry modules (Hopkins et al. 2023). They coevolve the gas, dust, and radiation temperature from the stellar luminosity and an external radiation field.

Sink particles represent individual stars. Once they form, they follow the subgrid protostellar evolution model in Offner et al. (2009). The STARFORGE framework includes stellar feedback from protostellar jets, radiation, stellar winds, and SNe. Feedback from SNe, radiation, and most stellar winds is injected by distributing mass, momentum, and energy into surrounding gas cells using the weighting scheme described in Hopkins et al. (2018). Feedback from protostellar jets and stellar winds, where the free-expansion radius is smaller than the size of a wind cell, is injected using the cell spawning technique described in Grudić et al. (2021).

Protostellar jets are modeled using the jet feedback model of Cunningham et al. (2011) in which sink particles launch a fraction of their accreted material $f_w$ along their rotational axis with a velocity that is a fraction $f_\mathrm{K}$ of the Keplerian velocity defined at the protostellar radius. We use $f_w = f_\mathrm{K} = 0.3$, which Rosen & Krumholz (2020) found reproduces measurements of momentum injection as a function of the protostellar luminosity (Maud et al. 2015). We do not include CR acceleration from protostellar jets.

Massive main-sequence stars inject a significant amount of energy and momentum into their environment through radiative feedback and stellar winds. Winds are launched for stars more massive than $2 M_\odot$. The stars lose mass isotropically at a mass-

**Table 1**
Initial Conditions of the Simulated Clouds

| $M_{\rm cloud}(M)$ | $R_{\rm cloud}$ (pc) | $\alpha_{\rm turb}$ | $\mu$ | $T_0$ (K) | $M_{\rm cloud}/\Delta m$ | $\Delta x_J$ (au) |
|---|---|---|---|---|---|---|
| $2\times10^3$ | 3 | 2 | 1.3 | 10 | $2\times10^6$ | 36 |

**Note.** Columns are the initial cloud mass, size, virial parameter, mass-to-magnetic-flux ratio, temperature, mass resolution, and minimum resolved Jeans length (Guszejnov et al. 2022).

loss rate $\dot{M}_w$ moving at velocity $v_w$. Wind mass-loss rates and velocities are calculated by Smith (2024; see Equation (1) of Grudić et al. 2022) and Lamers et al. (1995; see Equation (45) of Grudić et al. 2021). The luminosity of the winds is $\dot{E}_w = 0.5\dot{M}_w v_w^2$. Typical wind luminosities are $\sim$0.1–10$L_\odot$ (or $\sim10^{40}$–$10^{42}$ erg yr$^{-1}$). Stellar winds with velocities $v_w > 1000$ km s$^{-1}$ inject 10% of their energy into CRs, consistent with estimates made from $\gamma$-ray measurements in massive star clusters (Aharonian et al. 2019; Pandey et al. 2024). The CR energy is injected by including an energy source term $S_e = 0.1\dot{E}_w$ and a momentum source term $S_{F_e} = S_e c(\hat{v_w}\cdot\hat{\boldsymbol{B}})$ parallel to the local magnetic field $\hat{\boldsymbol{B}}$ in the CR transport equations (Section 2.2.1). To satisfy conservation of energy the wind velocity is reduced to $v_w \rightarrow \sqrt{0.9}\,v_w$. All of our calculations form sufficiently massive stars such that CRs are injected into the domain.

The STARFORGE framework also includes SNe, which are spawned at the end of the lifetime of main-sequence stars $>8M_\odot$. However, all our simulations end before SNe occur.

#### 2.1.2. Initial Cloud Properties

Our initial cloud properties are similar to those used in previous STARFORGE simulations (Grudić et al. 2021, 2022; Guszejnov et al. 2021, 2022). We start with a cloud of gas with mass $M_{\rm cloud} = 2000M_\odot$ and radius $R_{\rm cloud} = 3$ pc at a uniform density of $\rho_{\rm cloud} = M_{\rm cloud}/(4\pi R_{\rm cloud}^3/3)$ and a uniform temperature $T_0 = 10$ K. The cloud is placed in a diffuse medium with a density of $\rho_{\rm cloud}/1000$, within a periodic box of size $10R_{\rm cloud}$. The initial velocity field is initialized so that the velocity power spectrum varies with the wavenumber as $E_k \propto k^{-2}$. Velocities are scaled to the value set by the turbulent virial parameter $\alpha_{\rm turb} = 2$, which measures the relative importance of turbulence and gravity (Bertoldi & McKee 1992; Federrath & Klessen 2012):

$$\alpha_{\rm turb} = \frac{5\sigma_{\rm 1D,cloud}^2 R_{\rm cloud}}{GM_{\rm cloud}}, \tag{1}$$

where $\sigma_{\rm 1D,cloud}$ is the line-of-sight velocity dispersion. The clouds have a uniform magnetic field $B_z$ set by the mass-to-flux ratio $\mu = 1.3$:

$$\mu = c_1\sqrt{\frac{E_{\rm mag}}{E_{\rm grav}}}, \tag{2}$$

where $E_{\rm mag}$ and $E_{\rm grav}$ are the magnetic and gravitational energy, respectively, and the normalization constant $c_1 \approx 0.4$ (Mouschovias & Spitzer 1976). We use a mass resolution of $10^{-3}M_\odot$ for gas cells, so each cloud initially consists of $2\times10^6$ gas cells. The minimum resolved Jeans length is $\Delta x_J = 36$ au.

Table 1 restates the cloud properties in our simulations. Throughout this study, we present results in terms of the cloud freefall time, defined as

$$t_{\rm ff} = \sqrt{\frac{3\pi}{32G\rho_{\rm cloud}}}, \tag{3}$$

which is $t_{\rm ff} \approx 2$ Myr. We run the simulations until the clouds are completely dispersed by feedback, which occurs at $\sim$8 Myr (or 4 $t_{\rm ff}$).

### 2.2. Cosmic-Ray Methodology

#### 2.2.1. Cosmic-Ray Transport

Our study extends the STARFORGE simulation suite by including the GIZMO module for "single-energy-bin" CRT. This evolves the CR total energy and flux directly, integrating over the CR spectrum, so it effectively represents the $\sim$0.5–10 GeV protons, which contain most of the CR energy and pressure. This CR treatment has been used extensively in the FIRE suite of cosmological simulations (Chan et al. 2019; Hopkins et al. 2020, 2021a, 2021b, 2021c, 2022a, 2022b, 2022c). The GIZMO implementation treats CRs as a relativistic fluid ($\gamma_{\rm cr} = 4/3$) obeying an appropriate set of fluid-like equations derived from the collisionless Vlasov equation. We use the treatment of CRs first formulated in Hopkins et al. (2022b), which integrates a set of moment equations using a reduced speed of light (RSOL) approximation. This method allows for anisotropic CR transport with streaming, advection, diffusion, and energy losses. We refer readers to Hopkins et al. (2022b) for a detailed derivation of the CRT equations and provide only the necessary details here.

We evolve the total CR energy $e_{\rm cr}$ and the CR energy flux $F_{e,\rm cr}$; note that $F_{e,\rm cr}$ is a scalar quantity describing the flux parallel to the local magnetic field; the cross-field flux is assumed to be zero. The expressions solved for $e_{\rm cr}$ and $F_{e,\rm cr}$ are given by

$$D_t e_{\rm cr} + \nabla\cdot(F_{e,\rm cr}\hat{\boldsymbol{B}}) = \tilde{S}_{\rm sc} + S_e - \Gamma_{\rm cr} - \Gamma_{\rm st} - \mathbb{P}_{\rm cr}\colon\nabla\boldsymbol{u}, \tag{4}$$

$$D_t F_{e,\rm cr} + c^2\,\hat{\boldsymbol{B}}\cdot(\nabla\cdot\mathbb{P}_{\rm cr}) = -\bar{\nu}_s[F_{e,\rm cr} - 3\chi_e v_{\rm st}(e_{\rm cr} + P_{\rm cr})] + S_{F_e}, \tag{5}$$

where $\boldsymbol{u}$ is the gas velocity, $\hat{\boldsymbol{B}}$ is the local magnetic field direction, $\mathbb{P}_{\rm cr} = 3P_{\rm cr}\,\mathbb{D}_{\rm cr}$ is the CR pressure tensor with a scalar pressure $P_{\rm cr} \approx e_{\rm cr}/3$, $\mathbb{D}_{\rm cr}$ is the Eddington tensor, $\bar{\nu}_s = \bar{\nu}_s^+ + \bar{\nu}_s^-$ is the total scattering rate from forward and backward scattering rates in the Alfvèn frame (related to the CR diffusion coefficient $D_\parallel = v_{\rm cr}^2/3\bar{\nu}_s$ discussed in Section 3.1.3), $v_{\rm cr} \approx c$ is the velocity of an individual CR particle, and $\chi_e$ is a closure variable (discussed further below). The streaming velocity $v_{\rm st}$ is approximated as the ion Alfvén speed $v_{\rm Ai} = B/\sqrt{4\pi\rho_{\rm ion}}$, where $\rho_{\rm ion} = \chi\rho_{\rm gas} = m_{\rm ion}nf_{\rm ion}$, $\chi = f_{\rm ion}m_{\rm ion}/m_p$ is the mass-weighted ionization fraction, $\rho_{\rm gas}$ is the total gas density, and $m_{\rm ion}$ and $f_{\rm ion}$ are the mean ion mass and ionization fraction by number, respectively.[6,7] The $\mathbb{P}_{\rm cr}\colon\nabla\boldsymbol{u}$ term in Equation (4) represents the

[6] Formally, the streaming speed is $[(\nu_+ - \nu_-)/(\nu_+ + \nu_-)]\,v_{\rm Ai}$ where the prefactor represents the fractional asymmetry in the forward/backward scattering rates. But for $\sim$ GeV in the limit of interest where the streaming speed is large (the case we explore here), this is almost always expected to be $\sim$1.

[7] The mean ion mass $m_{\rm ion}$ is approximated as $m_{\rm ion} = m_p$, which is equivalent to setting $\chi = f_{\rm ion}$. This is not accurate in MCs where the dominant charge carrier is $HCO^+$ ($m_{\rm ion} = 29m_p$; Krumholz et al. 2020); however, since the CRT is calculated assuming $m_{\rm ion} = m_p$, for consistency we make this assumption throughout this study for analysis. We discuss the implications of this in Section 4.3.4.

adiabatic compression of CRs with the gas. The term $\tilde{S}_{\rm sc} = (\bar{v}_s/c^2)3\chi_e v_{\rm Ai}^2(e_{\rm cr} + P_{\rm cr})$ represents diffusive reacceleration. The $S_e$ and $S_{F_e}$ terms represent sources of CR energy and momentum, respectively, which in our simulations are only CR injections from stellar winds. The $\Gamma_{\rm cr}$ and $\Gamma_{\rm st} = -(\bar{v}_s/c^2)v_{\rm st}F_{e,\rm cr}$ terms represent collisional and streaming instability energy losses, respectively, which are discussed further in Section 2.2.3. Finally, the $-\bar{v}_s F_{e,\rm cr}$ and $\bar{v}_s 3\chi_e v_{\rm st}(e_{\rm cr} + P_{\rm cr})$ terms in Equation (5) represent scattering and streaming, respectively, where the latter arises if the scattering is asymmetric.

The Eddington tensor $\mathbb{D}_{\rm cr} = \chi_e \mathbb{I} + (1 - 3\chi_e)\hat{\boldsymbol{B}}\hat{\boldsymbol{B}}$ is defined in terms of the variable $\chi_e = (1 - \langle\mu_f^2\rangle)/2$, where a closure relation is used for $\langle\mu_f^2\rangle$ to provide a complete system of equations. Hopkins et al. (2022b) assume a closure relation analogous to that adopted in radiation hydrodynamics (Levermore 1984), which is a function that smoothly interpolates between the diffusive and streaming limits:

$$\langle\mu_f^2\rangle \approx \frac{3 + 4\langle\mu_f^1\rangle^2}{5 + 2(4 - 3\langle\mu_f^1\rangle^2)^{1/2}}, \tag{6}$$

where $\langle\mu_f^1\rangle = F_{e,\rm cr}/v_{\rm cr}e_{\rm cr}$. In the diffusive limit, $\langle\mu_f^1\rangle = 0$ and $\langle\mu_f^2\rangle = 1/3$, so $\chi_e = 1/3$. In the free streaming limit, $\langle\mu_f^1\rangle = 1$ and $\langle\mu_f^2\rangle = 1$, so $\chi_e = 0$.

#### 2.2.2. Coupled Gas and Cosmic-Ray Equations of Motion

Since CRs exchange energy and momentum with the gas via scattering and Lorentz forces (Zweibel 2013, 2017; Hopkins et al. 2022b), the default GIZMO momentum and energy equations must be modified to account for the influence of CRs. Spatial differences in the CR pressure tensor $\nabla \cdot \mathbb{P}_{\rm cr}$ produce a net CR current. The current parallel to $\hat{\boldsymbol{B}}$ is resisted only by exchanging momentum with the gas; therefore, the force balances the scattering + streaming term in Equation (5). The perpendicular current is redirected by Lorentz forces that exert an equal and opposite force on the gas, which is $\approx -\nabla_\perp \cdot \mathbb{P}_{\rm cr}$ (Zweibel 2017; Hopkins et al. 2022b), where for convenience we have introduced the shorthand notation $\nabla_\parallel \cdot \mathbb{Q} \equiv \hat{\boldsymbol{B}}(\nabla \cdot \mathbb{Q})$ and $\nabla_\perp \cdot \mathbb{Q} \equiv \nabla \cdot \mathbb{Q} - \nabla_\parallel \cdot \mathbb{Q}$ for any quantity $\mathbb{Q}$. Using Equation (5), the final modified momentum equation can be written as

$$D_t(\rho\boldsymbol{u}) + \ldots + \nabla \cdot \mathbb{P}_{\rm cr} = \hat{\boldsymbol{B}}(\nabla \cdot \mathbb{P}_{\rm cr}) + \left(\frac{\hat{\boldsymbol{B}}}{c^2}\right)\bar{v}_s[F_{e,\rm cr} - 3\chi_e v_{\rm st}(e_{\rm cr} + P_{\rm cr})], \tag{7}$$

where … refers to all non-CR terms. This has a pressure gradient term and a source term that vanishes when the flux is in a steady state.

The modifications to the energy equation balance the CR energy gains and losses. These include CR energy losses due to work done on the gas outlined in Equation (7) along with the four gain and loss terms shown in Equation (4) (energy gained from diffusive reacceleration, CR energy injection, energy lost due to streaming, and collisional and noncollisional losses). Collecting all these terms, the final modified energy equation is

$$D_t(e_{\rm tot}) + \ldots = \boldsymbol{u} \cdot D_t(\rho\boldsymbol{u})|_{\rm cr} + \Gamma_{\rm st} + S_{\rm gas} - \tilde{S}_{\rm sc} - S_e, \tag{8}$$

where $e_{\rm tot} = e_{\rm kin} + e_{\rm mag} + e_{\rm rad} + e_{\rm int}$ is the sum of the gas kinetic, magnetic, radiation, and internal energies, $D_t(\rho\boldsymbol{u})|_{\rm cr}$ is the CR term on the right side of Equation (7), and $S_{\rm gas}$ is the gas heating term due to CR collisional energy losses (described in Section 2.2.3).

#### 2.2.3. Energy Loss Processes

While they propagate, CRs lose energy due to interactions with nonrelativistic particles. Here we adopt an estimate for combined hadronic, Coulomb, and ionization losses. The hadronic/Coulomb losses are from Völk et al. (1996) and Ensslin et al. (1997) and are updated in Guo & Oh (2008). The total CR energy loss rate due to these processes is $\Lambda_{\rm cr} = \Lambda_{\rm coul} + \Lambda_{\rm had} + \Lambda_{\rm ion}$,

$$\Lambda_{\rm cr} = 7.51 \times 10^{-16}(1 + 0.22\tilde{n}_e + 0.125f_{\rm neut})\left(\frac{n_{\rm H}}{\rm cm^{-3}}\right){\rm s}^{-1}, \tag{9}$$

where $n_{\rm H}$ is the hydrogen number density, $\tilde{n}_e$ is the number of free electrons per hydrogen nucleus, and $f_{\rm neut} = (1 - f_{\rm ion})$ is the neutral gas fraction. The energy loss term in Equation (4) is then $\Gamma_{\rm cr} = \Lambda_{\rm cr}e_{\rm cr}$. Following Guo & Oh (2008), we assume 1/6 of the hadronic losses and all nonhadronic losses are thermalized, adding a volumetric heating component to the gas

$$\Lambda_{\rm gas} = 7.51 \times 10^{-16}(0.17 + 0.22\tilde{n}_e + 0.125f_{\rm neut}) \times \left(\frac{n_{\rm H}}{\rm cm^{-3}}\right){\rm s}^{-1}. \tag{10}$$

The gas heating rate in Equation (8) is then $S_{\rm gas} = \Lambda_{\rm gas}e_{\rm cr}$.

The CRs also lose energy due to the streaming instability. As they stream, CRs excite Alfvèn waves caused by anisotropy in the CR distribution. This drives the CRs to stream down the CR pressure gradient and effectively travel at the ion Alfvèn speed. The CR energy is transferred to the waves, which are quickly thermalized and heat the gas (Kulsrud & Pearce 1969; Skilling 1975). CR streaming losses are parameterized in Equation (4) by the term $\Gamma_{\rm st}$. We describe the magnitude and impact of these losses in more detail in Section 4.1.1.

#### 2.2.4. Reduced Speed of Light Approximation

Explicitly integrating Equations (4) and (5) imposes a Courant-type time-step limiter $\Delta t \leqslant C\Delta x/c$, which is numerically prohibitive because $c$ is significantly faster than any other speed in the problem. Therefore, analogously to radiation hydrodynamics, we adopt an RSOL approximation, which has been done in many previous CR studies (Jiang & Oh 2018; Chan et al. 2019; Hopkins et al. 2020). Following Hopkins et al. (2022b), we use an RSOL approximation for Equations (4) and (5) equivalent to replacing $c^{-1}D_t e_{\rm cr} \rightarrow \tilde{c}^{-1}D_t e_{\rm cr}$ and $c^{-1}D_t(F_{e,\rm cr}/c) \rightarrow \tilde{c}^{-1}D_t(F_{e,\rm cr}/c)$ in the original CR transport equation:

$$\frac{1}{\tilde{c}}D_t e_{\rm cr} + \nabla \cdot \left(\frac{F_{e,\rm cr}}{c}\hat{\boldsymbol{B}}\right) = \frac{1}{c}(\tilde{S}_{\rm sc} + S_e - \Gamma_{\rm cr} - \Gamma_{\rm st} - \mathbb{P}_{\rm cr}\colon \nabla\boldsymbol{u}), \tag{11}$$

$$\frac{1}{\tilde{c}}D_t\left(\frac{F_{e,\mathrm{cr}}}{c}\right)+(\nabla\cdot\mathbb{P}_{\mathrm{cr}})$$
$$=\left(\frac{-\bar{\nu}_s}{c^2}\right)[F_{e,\mathrm{cr}}-3\chi_e v_{\mathrm{st}}(e_{\mathrm{cr}}+P_{\mathrm{cr}})]+\left(\frac{1}{c^2}\right)S_{F_e}. \quad (12)$$

We use a value of $\tilde{c}=300\,\mathrm{kms}^{-1}$ in our simulations, which is justified through a low-resolution convergence study presented in the Appendix.

The STARFORGE simulations also use an RSOL approximation in the radiation flux equation (Grudić et al. 2021). The default STARFORGE RSOL for radiation is either $30\,\mathrm{km\,s}^{-1}$ (Grudić et al. 2021, 2022) or $90\,\mathrm{km\,s}^{-1}$ (Grudić et al. 2023); however, in these runs, we set $\tilde{c}=300\,\mathrm{kms}^{-1}$ for radiation for consistency since it does not increase the computational cost. We note that adopting a higher RSOL is primarily important for accurately capturing the optically thick, strong-radiation field limits characteristic of massive star formation (Skinner & Ostriker 2013).

#### 2.2.5. Cosmic-Ray Diffusion Coefficient–Constant Coefficient Case

The key ingredient in our CR evolution equations that we have not yet specified is the value of the diffusion coefficient $D_{\parallel}$; the value of this parameter is, as discussed in Section 1, crucial to the outcome. For our fiducial simulations, we adopt a diffusion coefficient $D_{\parallel}$ that is constant spatially and temporally.

We derive the diffusion coefficient following Sampson et al. (2023), where the authors use an ensemble of MHD turbulence simulations to quantify how the basic parameters describing ISM turbulence affect the transport of streaming CRs. They make the assumption that the total scattering rate $\bar{\nu}_s$ is extremely large (driven by the CR streaming instability) and also asymmetric. In these limits, $v_{\mathrm{st}}\rightarrow v_{\mathrm{Ai}}$ (Section 2.2.1) so that streaming dominates the CR transport and the microphysical diffusion coefficient $D_{\parallel,\mathrm{micro}}=c^2/3\bar{\nu}_s$ arising from CR pitch-angle scattering is negligibly small in comparison to the effective diffusion coefficient induced by random walk of magnetic field lines (and related processes) due to unresolved turbulence. Under this assumption, they derive a macroscopic diffusion coefficient $D_{\parallel,\mathrm{FLW}}$ that quantifies this process; the model is effectively a large eddy simulation closure for CR transport.

Since $D_{\parallel,\mathrm{FLW}}$ does not arise from CR pitch-angle scattering, it and $D_{\parallel,\mathrm{micro}}$ cannot be formally added together in Equations (4) and (5) (there is no scattering rate $\bar{\nu}_s$ that can be derived from the two that can then be used to obtain a total diffusion coefficient using $\bar{\nu}_s=c^2/3D_{\parallel}$). However, as long as Equation (5) is in a steady state ($D_tF_{e,\mathrm{cr}}\rightarrow 0$) all terms appear as they should. In our simulations, Equation (5) reaches equilibrium on a timescale $\Delta t_{\mathrm{F}}\sim(c/\tilde{c})\bar{\nu}_s^{-1}\sim 10$ yr (Hopkins et al. 2021a), which is much shorter than the macroscopic timescales we consider. Finally, since $D_{\parallel,\mathrm{FLW}}$ is derived under the assumption that $D_{\parallel,\mathrm{FLW}}\gg D_{\parallel,\mathrm{micro}}$ (and we show in Section 2.2.6 that this is a valid assumption), we arrive at $D_{\parallel}\sim D_{\parallel,\mathrm{FLW}}$.

The diffusion coefficient of interest here is measured on the minimum size scale $l_{\mathrm{min}}$ that is resolved by our simulations since processes on larger scales are presumably resolved directly. Since GIZMO is a Lagrangian method, the spatial resolution varies throughout the simulation according to the local conditions. Therefore, we estimate $l_{\mathrm{min}}$ based on the dynamic range of the cloud's turbulent power spectrum. The minimum resolved length scale for a turbulent sphere is given by $l_{\mathrm{min}}=R_{\mathrm{cloud}}/k_{\mathrm{max}}$, where $k_{\mathrm{max}}=N_{\mathrm{1D}}/N_{\mathrm{cells,eff}}$ is the maximum wavenumber of the turbulence, $N_{\mathrm{1D}}=(N_{\mathrm{gas}}/(4\pi/3))^{1/3}$ is the 1D resolution of the simulation and $N_{\mathrm{cells,eff}}$ is the minimum number of cells required to resolve a turbulent mode. For our simulations, $N_{\mathrm{gas}}=2\times10^6$ and $N_{\mathrm{cells,eff}}\approx 10$, which gives $l_{\mathrm{min}}=0.38$ pc.

Sampson et al. (2023) present empirical fits for the parallel and perpendicular diffusion coefficient as a function of the plasma parameters to be used as subgrid recipes in simulations. We use the initial cloud magnetic field value $B\approx 7\mu$G and average gas density $\rho_{\mathrm{cloud}}\approx 18M_{\odot}/\mathrm{pc}^3$. For the ionization fraction, we adopt $\chi=10^{-7}$, which is within the range of observed values for Milky Way MCs (Caselli et al. 1998; Williams et al. 1998). For the velocity dispersion, we adopt the observed velocity dispersion for turbulent MCs (McKee & Ostriker 2007)

$$\sigma_{\mathrm{1D}}=0.9\left(\frac{l_{\mathrm{min}}}{1\mathrm{pc}}\right)^{0.56}\mathrm{km\,s}^{-1}, \quad (13)$$

which gives $\sigma_{\mathrm{1D}}\approx 0.53\,\mathrm{km\,s}^{-1}$. Finally, we assume Gaussian diffusion (where the CR distribution function follows $\partial f/\partial t=D_{\mathrm{FLW}}\nabla^2 f$), which is predicted for the characteristics of our problem. Following Sampson et al. (2023), we obtain values for the parallel and perpendicular diffusion coefficients of $D_{\parallel,\mathrm{FLW}}\approx 8.33\times10^{25}\,\mathrm{cm}^{-2}\,\mathrm{s}^{-1}$ and $D_{\perp,\mathrm{FLW}}\approx 4.3\times10^{22}\,\mathrm{cm}^{-2}\,\mathrm{s}^{-1}$. Since $D_{\perp,\mathrm{FLW}}\ll D_{\parallel,\mathrm{FLW}}$, we assume $D_{\perp,\mathrm{FLW}}=0$ and adopt $D_{\parallel,\mathrm{FLW}}$ as the constant value of the diffusion coefficient.

We note that these derived diffusion coefficients are much lower than the average galactic diffusion coefficient $D_{\mathrm{obs}}\sim10^{28}\,\mathrm{cm}^{-2}\,\mathrm{s}^{-1}$ derived from CR data (Evoli et al. 2019) for two reasons. First, we resolve CR streaming explicitly in the CR transport equations, while the observed diffusion coefficient arises from both scattering and unresolved streaming ($D_{\mathrm{obs}}=D_{\parallel}+v_{\mathrm{st}}\ell_{\mathrm{cr}}$). Additionally, $D_{\mathrm{obs}}$ is measured in the ionized ISM where $D_{\parallel,\mathrm{FLW}}\ll D_{\parallel,\mathrm{micro}}$. The magnitude of $D_{\parallel,\mathrm{FLW}}$ is orders of magnitude smaller when $f_{\mathrm{ion}}\sim 1$ compared to where $f_{\mathrm{ion}}\sim10^{-7}$ as in MCs (Sampson et al. 2023); in contrast when $f_{\mathrm{ion}}\sim 1$, $D_{\parallel,\mathrm{micro}}$ arises from a different pitch-angle scattering mechanism and is much larger. In principle, $D_{\parallel,\mathrm{micro}}$ arises from CR pitch-angle scattering off both the Alfvèn waves self-generated by the streaming instability and the extrinsic ISM turbulence ($\bar{\nu}_s=\bar{\nu}_s^{\mathrm{sc}}+\bar{\nu}_s^{\mathrm{et}}$). Sampson et al. (2023) assume $\bar{\nu}_s^{\mathrm{sc}}\gg\bar{\nu}_s^{\mathrm{et}}$, and that $\bar{\nu}_s^{\mathrm{sc}}$ is so large that the corresponding diffusion coefficient $D_{\parallel,\mathrm{micro}}\sim D_{\mathrm{sc}}$ is negligibly small; we show in Section 2.2.6 that this is a reasonable assumption in MCs. In contrast, in higher ionization environments CR scattering is dominated by resonant interactions with extrinsic turbulence (Xu & Lazarian 2017; Krumholz et al. 2020), so $\bar{\nu}_s^{\mathrm{et}}\gg\bar{\nu}_s^{\mathrm{sc}}$ and $D_{\parallel,\mathrm{micro}}\sim D_{\mathrm{obs}}\sim D_{\mathrm{et}}$ (Krumholz et al. 2020). In short, $D_{\mathrm{obs}}$ cannot be compared to either the value $D_{\parallel,\mathrm{FLW}}$ derived in this section or the value of $D_{\parallel,\mathrm{micro}}$ derived in Section 2.2.6.

In addition to our derived value of $D_{\parallel,\mathrm{FLW}}$, we explore the impact of varying $D_{\parallel,\mathrm{FLW}}$ by an order of magnitude. We also run simulations with a nonuniform CR diffusion coefficient, which we describe in Section 2.2.6. Our full suite of simulations, including the diffusion coefficient used for each, is described in Table 2.

**Table 2**
Details of the Variations We Use in the Initial Conditions and Physics of Our Simulations

| Simulation | $M_{\rm cloud}[M_\odot]$ | $\epsilon_{\rm cr,med}[{\rm eV\ cm^{-3}}]$ | $D_{\parallel}[{\rm cm^2\ s^{-1}}]$ |
|---|---|---|---|
| M2e3_E1_D8e25 | $2\times10^3$ | 1 | $8.33\times10^{25}$ |
| M2e3_noCRT | $2\times10^3$ | 0 | N/A |
| M2e3_E10_D8e25 | $2\times10^3$ | 10 | $8.33\times10^{25}$ |
| M2e3_E1_D8e24 | $2\times10^3$ | 1 | $8.33\times10^{24}$ |
| M2e3_E1_D8e26 | $2\times10^3$ | 1 | $8.33\times10^{26}$ |
| M2e3_E1_DVAR | $2\times10^3$ | 1 | Variable |

**Note.** Columns are the simulation name, cloud mass, initial CR energy density (outside the cloud), and CR diffusion coefficient.

#### 2.2.6. Cosmic-Ray Diffusion Coefficient–Variable Coefficient Case

In addition to running simulations with a constant CR diffusion coefficient, we also perform one simulation with a CR diffusion coefficient that varies spatially and temporally. Unlike the diffusion coefficient described in Section 3.1.3, which assumes CRT is dominated by streaming and the CR scattering rate $\bar{\nu}_s$ is large ($D_{\parallel,\rm micro} \ll D_{\parallel,\rm FLW}$), this simulation calculates the microphysical diffusion coefficient $D_{\parallel,\rm micro}$ self-consistently based on the local gas and CR properties and neglects field-line wandering ($D_{\parallel,\rm FLW} \rightarrow 0$). This has the advantage that it *predicts* whether CRs should be in the streaming-dominated limit rather than beginning with that postulate. It should also correctly model "ballistic" CR transport where $\bar{\nu}_s$ is small enough that CR scattering is entirely negligible for the entire CR trajectory and the CRs free stream down field lines through the cloud.

We use a model for the microphysical diffusion coefficient included in GIZMO which encapsulates CR pitch-angle scattering off both the Alfvèn waves self-generated by the streaming instability and scattering off extrinsic ISM turbulence ($\bar{\nu}_s = \bar{\nu}_s^{\rm sc} + \bar{\nu}_s^{\rm et}$; Hopkins et al. 2022c). For the extrinsic turbulence scattering component $\bar{\nu}_s^{\rm et}$, we use the default model from Hopkins et al. (2022c). We find in our simulations that in low-ionization environments such as starburst galaxies and MCs, efficient ion-neutral damping prevents extrinsic ISM turbulence from cascading down to the scales of CR gyroradii (Krumholz et al. 2020), and so this contribution is largely negligible.

Instead, CRT is dominated by streaming along field lines at the streaming speed $v_{\rm st}$, which is the ion Alfvèn speed and is modeled directly in the streaming terms in Equations (4) and (5). In a steady state, the wave damping rate $\Gamma_{\rm damp}$ induced by ion-neutral damping and other various damping mechanisms must be matched by the growth rate of the streaming instability $\Gamma_{\rm SI}$ (Hopkins et al. 2022c). The bulk CR propagation speed is $v_D = v_{\rm st} + v_{\rm diff} = v_{\rm Ai} + v_{\rm diff}$, where $v_{\rm diff}$ is the diffusive velocity component that arises from scattering off the CR-induced Alfvèn waves and $D_{\rm sc} \propto v_{\rm diff}$ is the corresponding diffusion coefficient. Since $\Gamma_{\rm SI} \propto v_D$, an increase in $\Gamma_{\rm damp}$ allows the CRs to propagate faster ($v_{\rm diff}$ and thus $D_{\rm sc}$ increase) until once again $\Gamma_{\rm damp} = \Gamma_{\rm SI}$. In other words, increased wave damping induces a finite scattering rate off the Alfvèn waves $\bar{\nu}_s^{\rm sc}$ with a diffusion coefficient $D_{\rm sc} = c^2/3\bar{\nu}_s^{\rm sc}$.

In general, the damping rate $\Gamma_{\rm damp}$ includes multiple damping mechanisms including ion-neutral, dust, linear Landau, and nonlinear Landau damping (with rates given in Hopkins et al. 2022c). In practice, here ion-neutral damping dominates and other sources of damping are negligible. The efficiency of ion-neutral damping depends on the local gas and CR properties and can create orders-of-magnitude variations in the CR diffusivity. The ion-neutral damping rate is $\Gamma_{\rm IN} = \nu_{\rm in}/2$, where $\nu_{\rm in}$ is the collision frequency between ions and neutrals; in a hydrogen-helium plasma this is approximated as

$$\Gamma_{\rm IN} \approx 10^{-9} f_{\rm neutral} \sqrt{\frac{T_{\rm gas}}{1000{\rm K}}} \left(\frac{\rho_{\rm gas}}{10^{-24}{\rm gcm^{-3}}}\right)\left(\frac{m_p}{m_{\rm ion}}\right){\rm s^{-1}}, \quad (14)$$

where $m_p$ is the proton mass, $m_{\rm ion}$ is the mean ion mass, $f_{\rm neutral} = (1 - f_{\rm ion})$ is the neutral gas fraction by number, $T_{\rm gas}$ is the gas temperature, and $\rho_{\rm gas} \approx \mu m_p n_{\rm gas}$ is the total gas density with mean molecular weight $\mu$ (Kulsrud & Pearce 1969; Bustard & Zweibel 2021; Hopkins et al. 2022c). The growth rate of the streaming instability is (Kulsrud 2005)

$$\Gamma_{\rm SI} \approx \alpha \Omega_{\rm ion} \left(\frac{n_{\rm CR}}{n_{\rm ion}}\right)\left(\frac{v_D}{v_{\rm Ai}} - 1\right), \quad (15)$$

where $n_{\rm ion} \approx f_{\rm ion}\rho_{\rm gas}/\mu m_p$ is the ion number density, $n_{\rm CR} \approx \epsilon_{\rm cr}/E_{\rm cr}$ is the CR number density for the CR energy density $\epsilon_{\rm cr}$ and characteristic energy of a CR particle $E_{\rm cr}$, $\Omega_{\rm ion} = eB/m_{\rm ion}c$ is the nonrelativistic ion frequency, and $\alpha \approx 1$ is a constant that depends on the details of the numerical integrals over nongyroresonant interactions. Setting $\Gamma_{\rm SI} = \Gamma_{\rm IN}$ and using $f_{\rm ion} \approx n_{\rm ion}/n_{\rm gas}$ and $E_{\rm cr} \sim 1{\rm GeV}$,

$$v_{\rm diff} \approx 300 v_{\rm Ai} f_{\rm ion} f_{\rm neut} \sqrt{\frac{T_{\rm gas}}{1000{\rm K}}} \left(\frac{\rho_{\rm gas}}{10^{-24}{\rm gcm^{-3}}}\right)^2 \times \left(\frac{B}{\mu G}\right)^{-1}\left(\frac{\epsilon_{\rm cr}}{\rm eV\ cm^{-3}}\right)^{-1}. \quad (16)$$

The diffusion coefficient $D_{\rm sc}$ is related to the diffusive component of the drift velocity as $D_{\rm sc} = v_{\rm diff}\ell_{\rm cr}$, where we define the CR gradient scale length $\ell_{\rm cr} = e_{\rm cr}/\nabla e_{\rm cr}$. The CR energy gradient $\nabla e_{\rm cr}$ is computed in GIZMO using a slope-limited, second-order least-squares gradient estimator (Hopkins 2015). Using typical cloud properties in MCs ($f_{\rm ion} \sim 10^{-7}$, $T \sim 10\,{\rm K}$, $\mu \approx 2.33$, $B \sim 10\mu G$, $n_{\rm gas} \sim 100\,{\rm cm^{-3}}$), $v_{\rm diff} \sim 0.05 v_{\rm Ai}(\epsilon_{\rm cr}/{\rm eVcm^{-3}})^{-1}$, so $D_{\rm sc} \sim 5\times 10^{26}(v_{\rm A,ideal}/10\,{\rm km\,s^{-1}})$ $(f_{\rm ion}/10^{-7})^{-1/2}(\epsilon_{\rm cr}/{\rm eVcm^{-3}})^{-1}(\ell_{\rm cr}/{\rm pc}){\rm cm^2 s^{-1}}$. The streaming component of the effective diffusion coefficient at larger scales (which we resolve directly in our simulations) is $v_{\rm Ai}\ell_{\rm cr} \sim 10^{28}(v_{\rm A,ideal}/10\ {\rm km\ s^{-1}})({\rm f_{ion}}/10^{-7})^{-1/2}(\ell_{\rm cr}/{\rm pc}){\rm cm^2 s^{-1}}$. Thus, although the streaming instability necessitates CR scattering, the CR transport is still dominated by streaming down field lines unless $\epsilon_{\rm cr} \ll 1\ {\rm eV\ cm^{-3}}$.

For our simulations, we set a lower limit of $8.33\times10^{24}\,{\rm cm^2\ s^{-1}}$ and an upper limit of $10^{34}\,{\rm cm^2\ s^{-1}}$ for $D_{\parallel,\rm micro}$. The upper limit is rarely used and makes little difference to our results, but the lower limit prevents regions outside of the cloud from using very low values of $D_{\parallel,\rm micro}$ that would cause the CRs to quickly lose all their energy before propagating into the cloud. Equation (14) shows that the ion-neutral damping rate outside the cloud can be low because of the high ionization fraction and low gas density; however, it is likely that in this regime there are other damping mechanisms that we are not accounting for (Hopkins et al. 2022c) because of our focus on the denser molecular gas.

Finally, we note that this model neglects $D_{\parallel,\rm FLW}$; none of our simulations consider both field-line wandering diffusion ($D_{\parallel,\rm FLW}$) and pitch-angle scattering diffusion ($D_{\parallel,\rm micro}$), since this is not easy to model mathematically. In this section, we have shown that the assumption that streaming dominates the

CR transport is valid ($v_{st} \gg v_{diff}$); however, the assumption that $D_{\parallel,micro} \ll D_{\parallel,FLW}$ used in Section 3.1.3 is not always the case. For the remainder of this study, we refer only to the diffusion coefficient $D_{\parallel}$ rather than distinguishing between the two.

#### 2.2.7. Initial CR Configuration

The simulations assume an initially uniform background $\epsilon_{cr,med}$ for the CR energy density in the diffuse medium outside the cloud. Integrating the CR flux spectrum in the solar neighborhood appropriately for the energy density and ionization rate gives values of $\epsilon_{cr} \approx 1$ eV cm$^{-3}$ and $\zeta \approx 1.6 \times 10^{-17}$ s$^{-1}$, respectively (Cummings et al. 2016; Stone et al. 2019); therefore, GIZMO assumes a CRIR of 1.6 $\times 10^{-17}$s$^{-1}$ per eV cm$^{-3}$. We choose our fiducial value of $\epsilon_{cr,med} = 1$ eV cm$^{-3}$ to be consistent with these measurements and previous measurements of CRIRs of $\zeta \approx 10^{-17}$ s$^{-1}$ in star-forming regions (Dalgarno 2006). Inside the cloud, we start with 10% of the medium CR energy density ($\epsilon_{cr,cloud} =$ 0.1 eV cm$^{-3}$) to reflect probable attenuation in the dense gas (Padovani et al. 2009, 2020). However, low-resolution tests show that the simulations progress similarly independently of whether the initial value is $\epsilon_{cr,cloud} = 1$ eV cm$^{-3}$ or 0.1 eV cm$^{-3}$.

Analytic calculations suggest that the CR energy density should be lower in MCs where the gas density is higher (Padovani et al. 2009); however, analysis of line-width observations along sight lines toward diffuse clouds have suggested a range of CRIRs that exceed this value (Indriolo & McCall 2012; Indriolo et al. 2015). The mean value in the Milky Way is $\zeta \approx 10^{-16}$ s$^{-1}$, an order of magnitude higher than the canonically assumed value (Indriolo et al. 2015). Additionally, higher ionization rates toward more active star-forming regions in the center of our galaxy, other galaxies (Behrens et al. 2022; Holdship et al. 2022; Rivilla et al. 2022), and toward SNRs (Ceccarelli et al. 2011) have been observed (see Padovani 2023 for a review). To reflect these uncertainties, we also perform one simulation with initial values of $\epsilon_{cr,med} = 10$ eV cm$^{-3}$ and $\epsilon_{cr,cloud} = 1$ eV cm$^{-3}$.

In total, we run six different simulations varying the CR diffusion coefficient and initial CR energy density. These are described in Table 2. We note that run M2e3_noCRT does not explicitly model CR transport but instead assumes a fixed CR energy density of $\epsilon_{cr} = 1$ eV cm$^{-3}$ (or a CRIR of $\zeta \approx 1.7 \times 10^{-17}$ s$^{1}$), which is used only to calculate the heating and cooling of the gas.

## 3. Results

### 3.1. Cloud Evolution

#### 3.1.1. Overview

We begin with a discussion of the cloud evolution for the fiducial cloud including CRT, M2e3_E1_D8e25, and a simulation with the same conditions, which assumes a uniform CRIR but no explicit CRT, M2e3_noCRT. Figure 1 shows the time evolution of the projected gas density, density-weighted gas temperature, density-weighted 1D velocity dispersion, and density-weighted CR energy density of the M2e3_E1_D8e25 run, with the positions of stars superimposed in blue. The 1D velocity dispersion for a cell is calculated from the $z$ component of the gas velocity $v_z$ as $\sigma_{1D} = \sqrt{(v_z - \bar{v_z})^2}$, where $\bar{v_z}$ is the mean value of $v_z$ for all cells along the line of sight. The evolution of the gas in the calculation including CRT follows a similar pattern to that of previous STARFORGE simulations (Guszejnov et al. 2021; Grudić et al. 2022; Guszejnov et al. 2022). At early times before star formation starts, the initial turbulence in the cloud leads to the formation of dense filaments, which host gravitationally unstable cores. By 1.9 Myr ($\approx t_{ff}$), some of the cores have collapsed and formed the first stars (column 1).

At $\sim$2.9 Myr ($\approx 1.5 t_{ff}$), the rate of star formation peaks (column 2). The forming protostars launch high-velocity outflows, which slow star formation and stir turbulence in the cloud. By 4.3 Myr ($\approx 2.2 t_{ff}$), massive stars ($>8 M_{\odot}$) launch stellar winds and produce bubbles of ionizing radiation. This creates a central cavity, which causes the surrounding gas to expand (column 3). By $2.5 t_{ff}$, feedback has completely disrupted the cloud and the cloud is dispersed.

The bottom row of Figure 1 follows the evolution of the CR energy density. The cloud boundary is clearly visible because the CR energy losses happen at a faster rate in the cloud material than in the external medium. However, the CR energy density is smoother and exhibits less filamentary substructure than the gas density. The evolution of the CR energy density inside the cloud is shown quantitatively in Figure 2, which plots the evolution of the median (solid) and mean (dashed) CR energy density as a function of time for various gas densities. Inside the cloud (blue, purple, and black lines), the CR energy density is lower and declines more steeply than outside the cloud (cyan); however, it is largely independent of gas density. The only significant variations before $\sim 1 t_{ff}$ are caused by artificial trapping in the dense gas (Appendix A), which creates slightly elevated median values in the high-density gas (black; Hopkins et al. 2020). The uniformity of the CR distribution indicates that CRs are losing most of their energy before penetrating into the filaments where stars are forming.

In all of our simulations, massive stars reach the minimum mass for stellar wind launching between $\sim$1.5 and $2 t_{ff}$. Except for in the M2e3_noCRT simulation, the massive stars inject CR energy and momentum as they lose mass (Section 2.1.1), causing the mean CR energy density in the cloud to rise. Many stars undergo accretion which rapidly increases their mass; consequently, the CR energy injected by each source is nearly constant or increasing. Figure 2 shows that by $\sim 1.75$–$2 t_{ff}$ there is enough CR injection to sharply increase the median CR energy density in the cloud, especially in the denser gas where the stars are forming (black). Once the stellar winds rarefy the gas the massive stars are no longer embedded, which causes the CR energy density in the dense gas to decline.

Finally, the dip in the median CR energy density at low densities (cyan) at $\sim 2.5 t_{ff}$ occurs because the cloud gas disperses faster than the CRs diffuse into this gas. The energy density dips to match the values at n $\gtrsim$500–10$^3$ cm$^{-3}$ (blue and purple), reflecting the CR levels in the regions previously at these gas densities. Once the background CRs stream into the low-density dispersing gas, the median CR energy density rises again.

For comparison, Figure 3 shows the evolution of the gas properties of the M2e3_noCRT run. In this simulation, a uniform CR heating rate is used that is equivalent to a CR energy density of $\epsilon_{cr} = 1$ eV cm$^{-3}$($S_{gas} = \Lambda_{gas} e_{cr} = \Lambda_{gas} \epsilon_{cr} / n_{cr}$ with $\Lambda_{gas}$ given in Equation (8)), while in the M2e3_E1_D8e25 run $\epsilon_{cr} < 1$ eV cm$^{-3}$ throughout most of the cloud. Figure 3 shows that despite the differences in the CRIRs between the

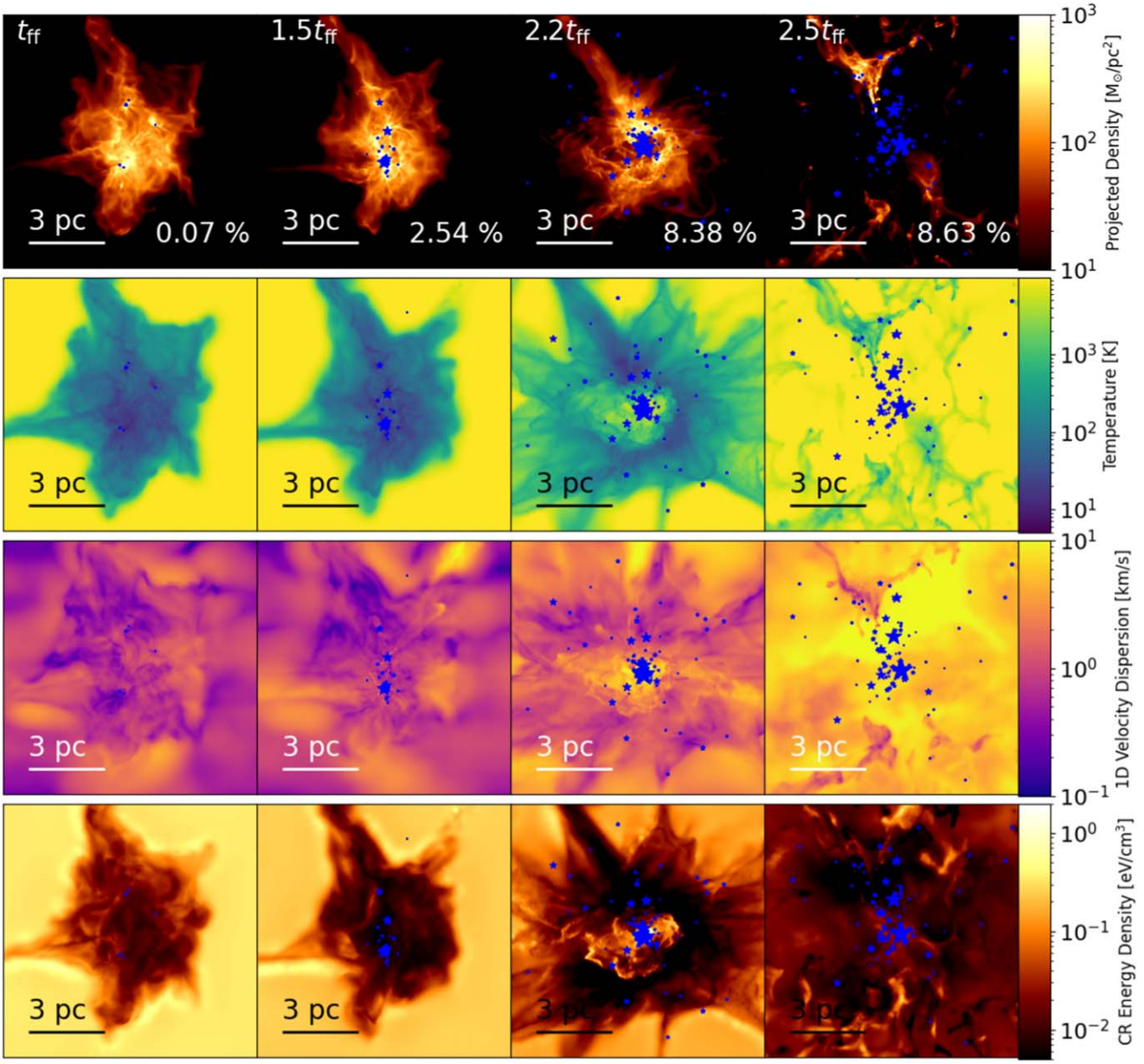


**Figure 1.** Projected density (top row), density-weighted temperature (second row), density-weighted 1D velocity dispersion (third row), and density-weighted CR energy density (bottom row) of the M2e3_E1_D8e25 simulation at four different times between $t_{ff} - 2.5t_{ff}$(∼2–5 Myr). The SFE at each time is given in the bottom right corner. Sink particles are plotted in blue, sized by their mass.

two runs, the effect of including CRT on the gas structure and overall star formation is minimal. Differences in the gas structure past ∼4 Myr can largely be attributed to variations in stellar feedback from the different sink particle distributions.

The effect of including CRT on the gas temperature and velocity dispersion is also minimal. Figure 4 shows the evolution of the median temperature (top) and velocity dispersion (bottom) as a function of time at various gas densities for all simulations. The velocity dispersion for a cell is calculated from the three components of the gas velocity $v_x$, $v_y$, and $v_z$ as $\sigma_{3D} = \sqrt{(v_x - \bar{v_x})^2 + (v_y - \bar{v_y})^2 + (v_z - \bar{v_z})^2}$, where $\bar{v_x}$, $\bar{v_y}$, and $\bar{v_z}$ are the mean values of $v_x$, $v_y$, and $v_z$, respectively, for all cells. Figure 4 shows the temperature in the M2e3_E1_D8e25 simulation (black) is actually a couple of degrees colder than the M2e3_noCRT simulation (cyan) due to the lower CR heating. Similarly, the median velocity dispersion for the two simulations is virtually identical until t $\approx t_{ff}$, indicating CRs are not significantly affecting the gas dynamics in the M2e3_E1_D8e25 run. Beyond t ≈1–1.5$t_{ff}$, the cloud begins to disperse due to feedback, and differences in these quantities are generally due to minor variations in the stellar mass distribution and cannot be attributed to CRs.

### 3.1.2. Star Formation in a High-CR Environment

We now compare the fiducial M2e3_E1_D8e25 CR simulation with the M2e3_E10_D8e25 simulation, which follows a cloud embedded in an environment with a 10 times higher initial CR energy density. The top two rows of Figure 5 show the projected CR energy density for all CRT simulations at t =1.5$t_{ff}$ (approximately the time of peak star formation). The CR energy density in the M2e3_E10_D8e25 cloud

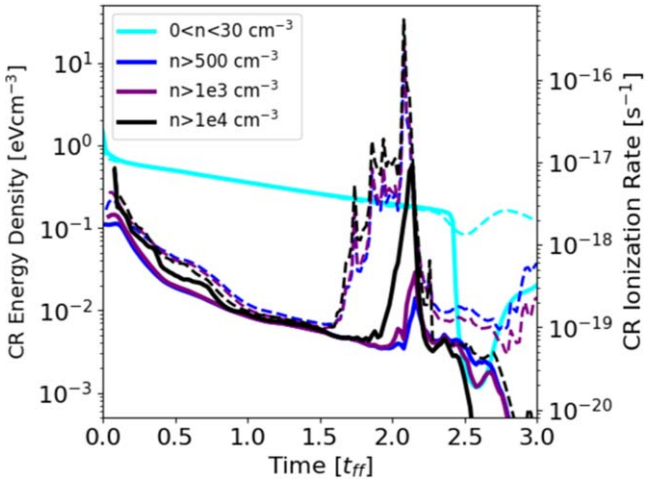


**Figure 2.** Median (solid) and mean (dashed) CR energy density (left axis) and the corresponding CRIR (right axis) for gas in the indicated density range or lower limit for the M2e3_E1_D8e25 simulation. The initial number density inside the cloud is $n_{\rm cloud} \approx 300\ {\rm cm}^{-3}$; therefore, we choose an upper cutoff of 30 $\rm cm^{-3}$ to represent gas outside the cloud. The cutoffs of 500 $\rm cm^{-3}$ and $10^3$ $\rm cm^{-3}$ are chosen from various definitions to define the cloud boundary, while $10^4$ $\rm cm^{-3}$ is a typical density of filamentary substructure and star formation.

declines at a similar rate to that of the M2e3_E1_D8e25 cloud. Despite the higher CR environment, the CR energy density inside the M2e3_E10_D8e25 cloud is relatively low, smaller than the typical 1 eV cm $^{-3}$ generally assumed for clouds. In both runs, by $t = 1.5 t_{\rm ff}$ the CR energy density in the cloud has declined by over an order of magnitude from its initial value, with values of $\epsilon_{\rm cr} \lesssim 10^{-2}$ eV $\rm cm^{-3}$ and $\epsilon_{\rm cr} \lesssim 10^{-1}$ eV $\rm cm^{-3}$ for the M2e3_E1_D8e25 and M2e3_E10_D8e25 clouds, respectively.

The higher CR energy does, however, affect the rate at which the cloud collapses and the time star formation commences. The bottom two rows of Figure 5 show the projected gas density for all simulations at $t = 1.5 t_{\rm ff} (\approx 3$ Myr). At this time, the M2e3_E10_D8e25 cloud (top right) is more compact and there are more stars compared to the M2e3_E1_D8e25 and M2e3_noCRT clouds (top left and middle, respectively). This occurs because the relatively high CR energy density outside the cloud acts as an additional pressure on the cloud. While this relative pressure imbalance does not appreciably affect the gas evolution in the M2e3_E1_D8e25 simulation, it is sufficient to accelerate the dynamical evolution of the cloud in the M2e3_E10_D8e25 simulation. Consequently, by $1.5 t_{\rm ff}$ more than twice as much of the cloud mass in the M2e3_E10_D8e25 run has formed (or been accreted onto) stars.

Although the higher CR background causes a faster initial collapse than in the fiducial M2e3_E1_D8e25 simulation, the other gas properties are qualitatively similar. The top panel of Figure 4 shows that the gas in the M2e3_E10_D8e25 simulation cools to a slightly lower median temperature than the M2e3_noCRT simulation (cyan) once the internal CR energy density declines. However, the cloud temperature is higher after $\sim 1\ t_{\rm ff}$ because the elevated star formation causes stronger and earlier heating. The bottom panel shows that the median gas velocity dispersion is also higher after $\sim 0.5\ t_{\rm ff}$, a consequence of the earlier star formation and subsequent impact of feedback within the cloud. Overall, due to the strong CR attenuation in the dense gas, star formation in the high-CR environment proceeds relatively similarly to star formation occurring in a typical CR environment.

#### 3.1.3. Impact of the CR Diffusion Coefficient on Star Formation

We now turn to a comparison with our simulations with different CR diffusion coefficients. The second row of Figure 5 shows the projected CR energy density at $t = 1.5\ t_{\rm ff}$ for the low diffusion coefficient M2e3_E1_D8e24, high diffusion coefficient M2e3_E1_D8e26, and variable diffusion coefficient M2e3_E1_DVAR simulations. The CR energy density in the cloud is even lower for the M2e3_E1_D8e24 (bottom left) run than for the M2e3_E1_D8e25 run, because the CRs scatter more, and consequently suffer greater attenuation by the time they are able to random-walk into the cloud interior. In the M2e3_E1_D8e26 run (bottom middle), the CRs scatter less frequently and lose comparatively little energy, so the cloud and medium reach an equilibrium value of $\epsilon_{\rm cr} \approx 1$ eV $\rm cm^{-3}$ (second-row middle panel of Figure 5).

The right panel in the second row of Figure 5 shows that the CR energy density in the M2e3_E1_DVAR simulation evolves qualitatively similarly to the M2e3_E1_D8e24 simulation. Computing the microphysical diffusion coefficient $D_{\parallel,\rm micro}$ typically gives lower average values than the value of $D_{\parallel,\rm FLW}$ used in the M2e3_E1_D8e25 simulation. Figure 6 (left) shows the median diffusion coefficient at different gas densities in the M2e3_E1_DVAR simulation. Outside the cloud (cyan line), the low gas densities and high ionization result in inefficient ion-neutral damping (Equation (14)) so the diffusion coefficient is typically equal to the minimum allowed value. Inside the cloud (purple and blue lines), the values of $D_{\parallel}$ increase as the cloud collapses because the higher densities create more efficient ion-neutral damping, which damps the Alfvèn waves and decreases the CR scattering rate. The right panel of Figure 6 shows a 2D histogram of the amplitude of the CR diffusion coefficient as a function of the gas density at $t = 0.5 t_{\rm ff}$. Before $\sim 1\ t_{\rm ff}$ the diffusion coefficient throughout most of the cloud is between the M2e3_E1_D8e25 value and the M2e3_E1_D8e24 value except at the highest gas densities. At densities $n < 1000\ {\rm cm}^{-3}$, a large fraction of the simulation space computes our lower cutoff value $D_{\parallel} = 8.33 \times 10^{24} {\rm cm}^2\ {\rm s}^{-1}$, which we impose due to the additional contribution of multiple wave damping mechanisms at lower gas densities (Section 2.2.6). For most of the cloud collapse, the high scattering rate causes the CRs to lose energy as in the M2e3_E1_D8e24 simulation.

For all three of these variations, the effect of CRT on the cloud evolution and gas properties is minimal. The bottom row of Figure 5 shows that the gas density at $t = 1.5\ t_{\rm ff}$ looks virtually identical to the gas density of the M2e3_E1_D8e25 cloud. As expected, the temperature of the M2e3_E1_D8e24 and M2e3_E1_DVAR simulations shown in Figure 4 (red and magenta, respectively) is lower than for the M2e3_E1_D8e25 simulation. The temperature in the M2e3_E1_D8e26 simulation is similar to that of the M2e3_E1_D8e25 simulation because both have a value of $\epsilon_{\rm cr} \approx 1$ eV $\rm cm^{-3}$ throughout the cloud. The velocity dispersion for all three is comparable since star formation proceeds similarly.

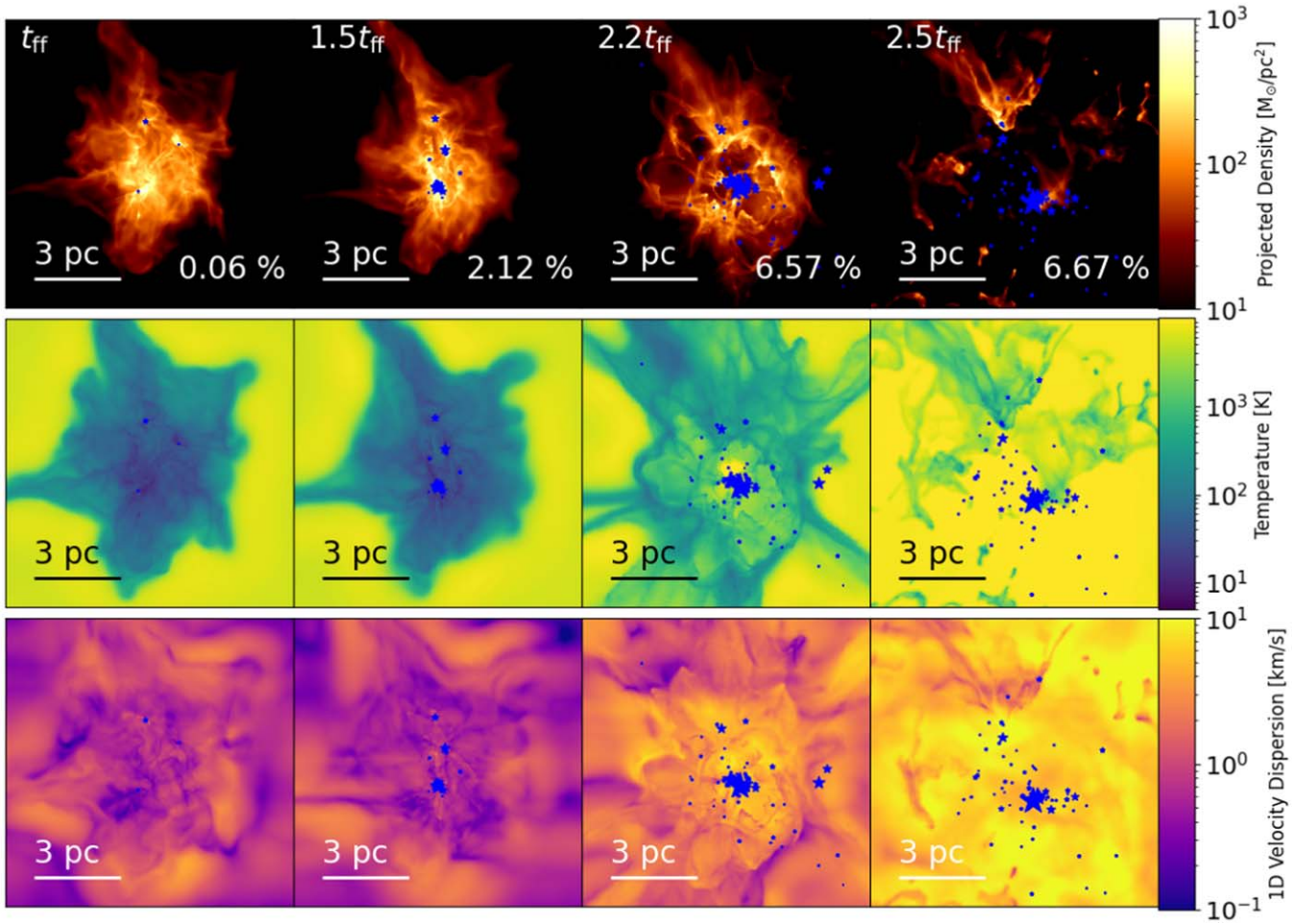


**Figure 3.** Same as Figure 1 except for the M2e3_noCRT simulation. In this simulation, a uniform CR energy density of $\epsilon_{cr} = 1$ eV cm$^{-3}$($\zeta \approx 2 \times 10^{-17}$ s$^{-1}$) is used in the heating and cooling functions.

### 3.2. Star Formation Properties

#### 3.2.1. Star Formation History of the Cloud

We now turn to various star formation metrics that can be obtained from the simulations and compared to observations. The star formation efficiency (SFE) is defined as the percentage of the initial cloud mass that has been converted to stars:

$$\mathrm{SFE}(t) = M_*(t)/M_0, \tag{17}$$

where $M_*(t)$ is the total stellar mass at time $t$. Figure 7, left, shows the evolution of the SFE for all runs. Qualitatively, the SFE evolves similarly in all cases. Once star formation starts, the SFE undergoes a period of rapid growth as the cloud collapses and the densities increase. The rate of star formation peaks at $\approx 1.5\, t_{ff}$. At this time, feedback begins to disperse the cloud, causing the slope of the SFE to decrease. By $\approx 2\, t_{ff}$, the SFE has plateaued and the cloud is dispersing.

Figure 7 shows that the inclusion of CRT does not have a significant impact on the star formation history of the cloud for any of our simulations with $\epsilon_{cr} = 1$ eV cm$^{-3}$. Up until $\approx 1.5\, t_{ff}$, the SFE looks very similar for all of these runs, and minor variations after this can be attributed to differences in star formation feedback. The SFE in the M2e3_E10_D8e25 cloud (blue lines) begins the period of steep rise slightly earlier than the other clouds due to the external CR pressure on the cloud discussed in Section 3.1.2; however, once star formation starts it proceeds at roughly the same rate for all of the clouds once the background CR level has declined. For all of our clouds, variations in the early evolution of the SFE are smaller than variations caused by different initial turbulent realizations with the same physics (Guszejnov et al. 2022).

To evaluate the significance of the variation between runs, we compare our results to a suite of 103 simulations of $M = 2000 M_\odot$ clouds evolved with different turbulent seeds and no CRT. 100 of these clouds were run with $E_{mag}/E_{grav} = 0.01$ and were presented in Grudić et al. (2023), while the other three were run with $E_{mag}/E_{grav} = 0.1$ but are otherwise identical. We take the mean value of the final SFE from the three higher-magnetization clouds plus our M2e3_noCRT run as the "standard" final SFE with no CRT and assume the standard deviation in the final SFE calculated from the suite of 100 lower magnetization clouds is representative of the variation. The $\pm 1\sigma$ region ($\mathrm{SFE} \approx 7.42 \pm 1.77$), is indicated as a gray shaded area in the left panel of Figure 7.

The second column of Table 3 shows the SFE at the final time $4\, t_{ff}$. The final SFE of our M2e3_noCRT cloud is the lowest. All of our $\epsilon_{cr} = 1$ eV cm$^{-3}$ clouds have slightly higher values, which could be due to the extra confining CR pressure; the M2e3_E1_D8e26 and M2e3_E1_DVAR are within $1\sigma$ while the M2e3_E1_D8e25 and M2e3_E1_D8e24 clouds are within $2\sigma$. The M2e3_E10_D8e25 cloud has a more than $2\sigma$ greater final SFE.

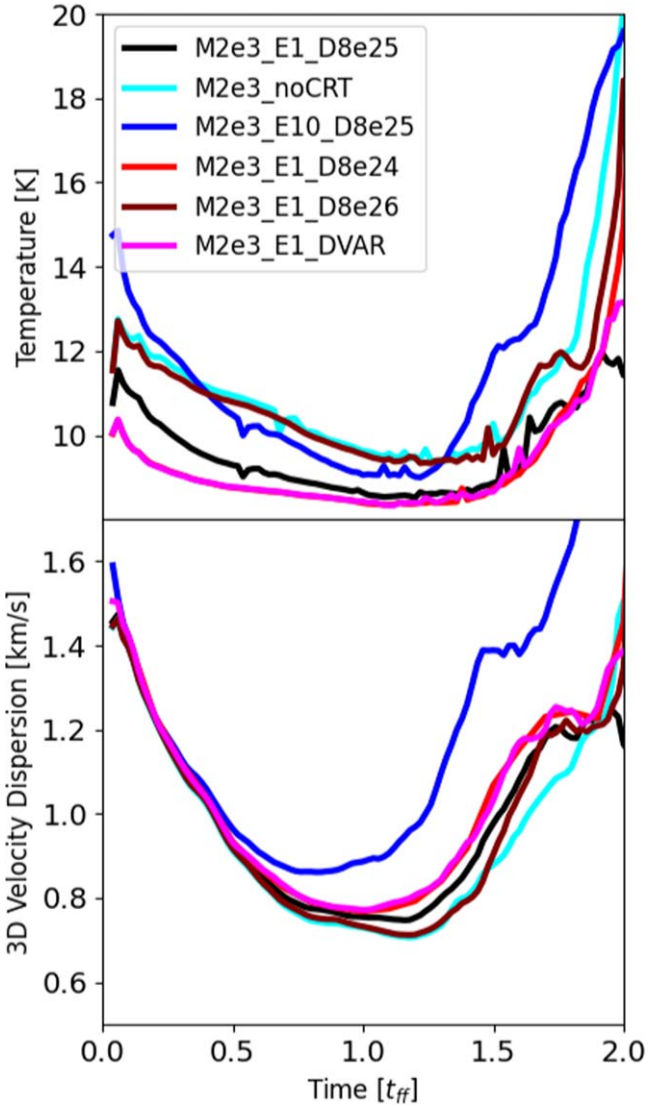


**Figure 4.** Median temperature(top) and median velocity dispersion (bottom) vs. time for all gas with number density $n > 1000\,\mathrm{cm}^{-3}$ for all simulations.

### 3.2.2. Final Stellar Mass Distribution

Figure 7, right, shows the evolution of the median mass of all sink particles with $M > 0.1M_{\odot}$. As in the left panel, the shaded region shows the mean of the final values from the four $E_{\mathrm{mag}}/E_{\mathrm{grav}} = 0.1$ simulations (including the M2e3_noCRT run) with the $1\sigma$ region from the 100 $E_{\mathrm{mag}}/E_{\mathrm{grav}} = 0.01$ simulations. There is no significant difference in the evolution of $M_{\mathrm{med}}$ between the CRT and M2e3_noCRT simulations, except for the M2e3_E1_D8e25 simulation. The median mass for that run experiences a sharp jump between $\sim$1.25 and 1.5 $t_{\mathrm{ff}}$ and then rises again sharply at $\sim$1.8 $t_{\mathrm{ff}}$. While the earlier jump may be due to statistical variation, the latter may be correlated with the CR injection by stellar winds discussed in Section 3.1, which was strongest in our M2e3_E1_D8e25 simulation. It occurs at approximately the same time as the sharp increase in the median CR energy density in the cloud from stellar wind injection shown in Figure 2. The additional CR energy may affect the gas temperature and pressure, which would affect the stellar mass distribution. A larger statistical study is required to draw firm conclusions.

The final value of $M_{\mathrm{med}}$ at $t = 4t_{\mathrm{ff}}$ is shown in the third column of Table 3. Except for the M2e3_E1_D8e25 simulation, all of our $\epsilon_{\mathrm{cr}} = 1\ \mathrm{eV\,cm}^{-3}$ runs are within $1\sigma$. The M2e3_E10_D8e25 simulation is slightly higher, within $2\sigma$.

At the final time, the $\epsilon_{\mathrm{cr}} = 1\ \mathrm{eV\,cm}^{-3}$ simulations have each formed $\sim$120–170 stars. Figure 8 shows the stellar mass distributions at $4t_{\mathrm{ff}}$ (left) and their normalized cumulative distribution functions (right). The shaded region represents the $1\sigma$ region in each mass bin from the 100 $E_{\mathrm{mag}}/E_{\mathrm{grav}} = 0.01$ simulations for a mass distribution with 136 stars and a high-mass slope $\alpha = -1$ in $dN/d\ln M$, shown by the gray dashed line. Qualitatively, the IMF for all of the $\epsilon_{\mathrm{cr}} = 1\ \mathrm{eV\,cm}^{-3}$ simulations appears reasonably well described by a Chabrier IMF (Chabrier 2005). Prior work indicates that protostellar jets are responsible for setting the mass scale of the IMF (Guszejnov et al. 2021). The high-mass slope is flatter than the canonical Chabrier value of $\alpha = -1.35$ but is consistent with previous STARFORGE simulations, which find $\alpha = -1$, possibly due to some missing physics, such as disk-mediated accretion and fragmentation, that enhance the number of massive stars (Grudić et al. 2022; Guszejnov et al. 2022). The peak of the M2e3_E1_D8e25 simulation is higher than that of the other simulations because of the higher median mass (Figure 7). Except for this, we find no qualitative difference between the IMFs of the $\epsilon_{\mathrm{cr}} = 1\ \mathrm{eV\,cm}^{-3}$ CRT simulations and the IMF of the M2e3_noCRT simulation.

The M2e3_E10_D8e25 simulation produced twice as many stars as the other simulations ($\sim$220). Figure 8 shows that the number of stars formed with $M \lesssim 0.1M_{\odot}$ is larger than the other simulations, resulting in a visual peak in the IMF at $\sim 0.1M_{\odot}$ rather than $\sim 0.3M_{\odot}$. However, the median mass of the M2e3_E10_D8e25 simulation above $0.1M_{\odot}$ is higher than all of the other simulations except the M2e3_E1_D8e25 simulation (Figure 7) because this simulation also formed more high-mass stars. Indeed, the high-mass slope of the M2e3_E10_D8e25 simulation in Figure 8 appears flatter than $\alpha = -1$ and the distribution is well outside the 1 $\sigma$ region at $M > 1M_{\odot}$. Higher-resolution simulations with a larger statistical sample of stars are required to confirm this trend.

### 3.3. Ionization

As shown in Figure 5, we find that in a Milky Way–like environment, for low to moderate values of the CR diffusion coefficient the CRIR is roughly uniform throughout the cloud. The median value ranges between $\zeta \approx 4 \times 10^{-20}$–$2 \times 10^{-19}\ \mathrm{s}^{-1}$ during the main star-forming epoch of the simulations ($t \approx 1 - 1.5t_{\mathrm{ff}}$). Figure 9 shows a phase plot of the total simulation mass as a function of the CR energy density and gas density at $1.5t_{\mathrm{ff}}$. The CRIR is shown on the right, which we calculate from the CR energy density assuming an ionization rate of $1.6 \times 10^{-17}\ \mathrm{s}^{-1}$ per $\mathrm{eV\,cm}^{-3}$ (Cummings et al. 2016). The blue line shows the mass-weighted mean CR energy density and corresponding CRIR at each gas density. The M2e3_E1_D8e25, M2e3_E1_D8e24, and M2e3_E1_DVAR clouds have a CRIR that strongly peaks at a value of $\sim 0.5 - 1 \times 10^{-19}\ \mathrm{s}^{-1}$, where some regions with $n < 10^4$ reach $\zeta \approx 10^{-18}\ \mathrm{s}^{-1}$. The M2e3_E1_D8e26 run has a nearly uniform CRIR of $\zeta \sim 10^{-17}\ \mathrm{s}^{-1}$ throughout the cloud.

The M2e3_E10_D8e25 simulation has elevated ionization rates throughout the cloud compared to the M2e3_E1_D8e25 simulation. The median value of the CRIR ranges from $\approx$1 to $6 \times 10^{-18}\ \mathrm{s}^{-1}$ between 1 and $1.5t_{\mathrm{ff}}$. Although the average CR

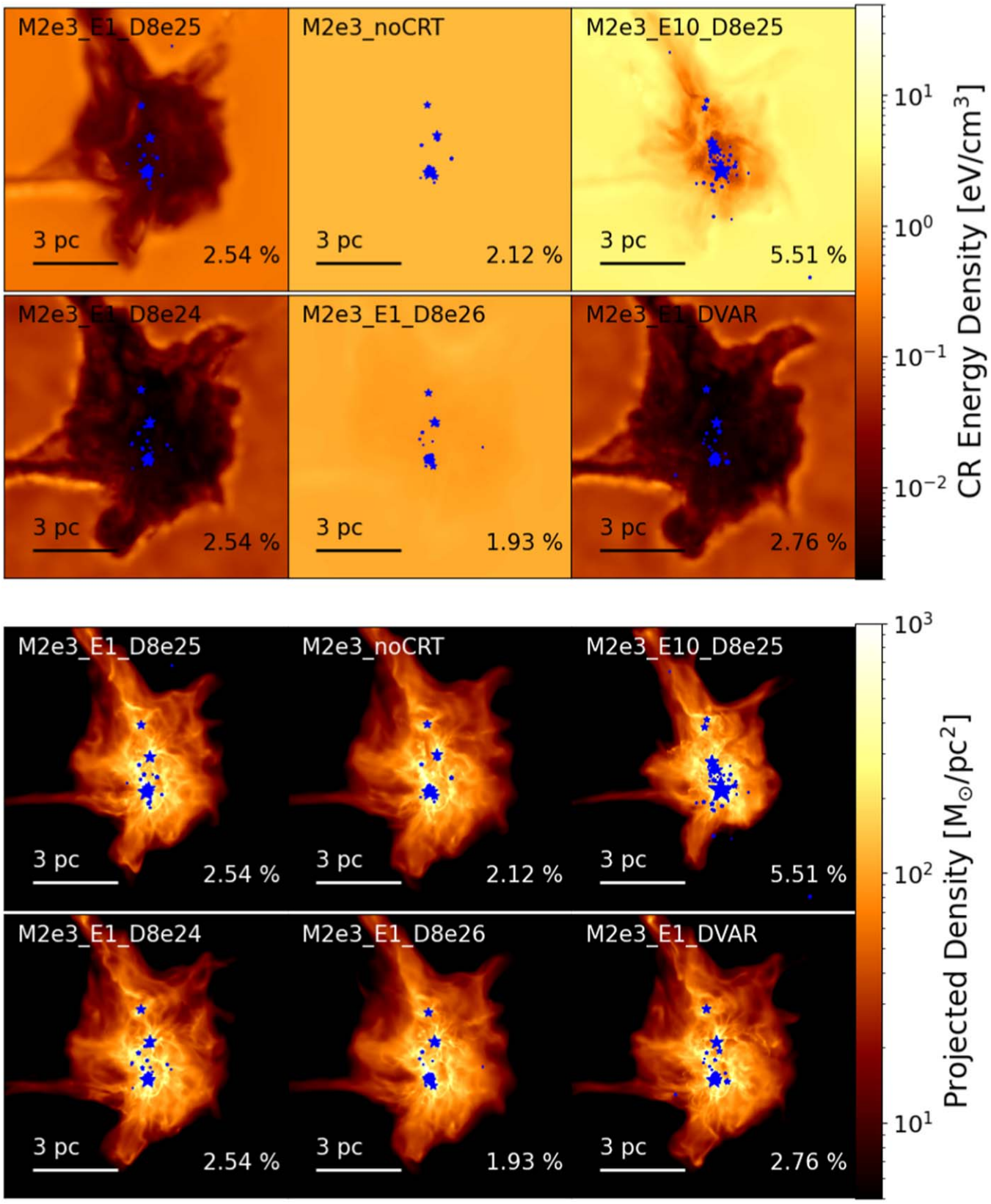


**Figure 5.** Top: density-weighted CR energy density for all simulations at $t = 1.5t_{\rm ff}(\approx 3$ Myr). Sink particles are plotted in blue, sized by their mass. The SFE at this time for each simulation is shown in the bottom right corner. For the M2e3_noCRT panel, a CR energy density of $\epsilon_{\rm cr} = 1$ eV cm$^{-3}$ is shown, corresponding to the assumed ionization rate of $\zeta \sim 1.7 \times 10^{-17}$ s$^{-1}$. Bottom: projected gas density for all simulations at $t = 1.5t_{\rm ff}(\approx 3$ Myr). Sink particle locations are indicated by blue stars, sized by their mass. The current SFE for each simulation is shown in the bottom right corner. Despite significant differences in the CR treatments, the star formation activity and distribution are qualitatively similar.

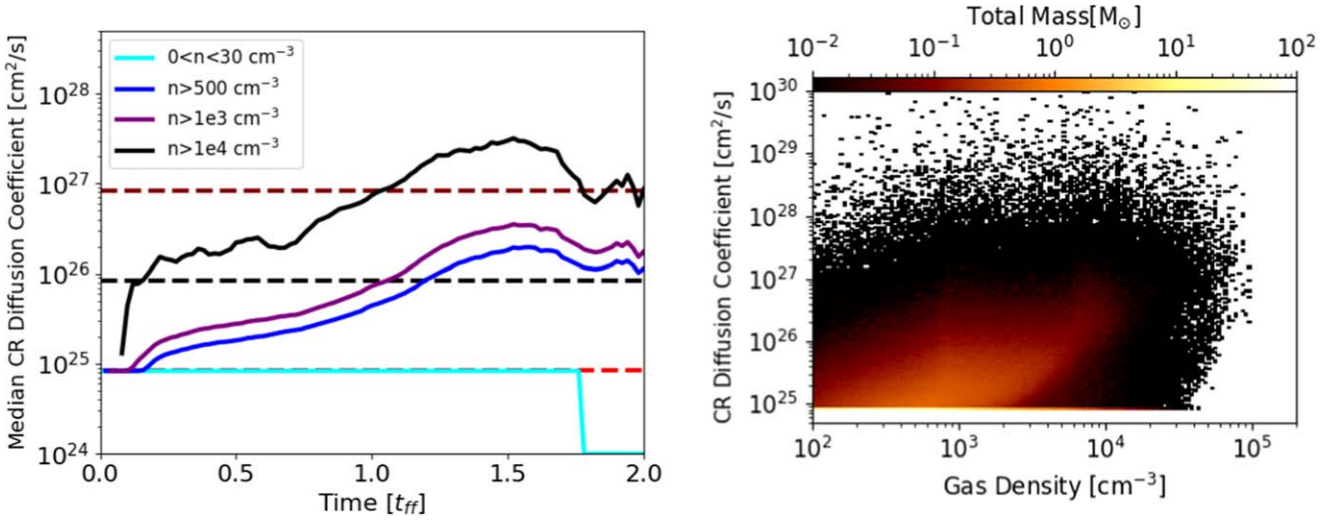


**Figure 6.** Left: median CR diffusion coefficient for gas cells in the indicated density range or lower limit for the M2e3_E1_DVAR simulation. Dashed horizontal lines show the constant values of the diffusion coefficient used in the M2e3_E1_D8e25 (black), M2e3_E1_D8e24 (red), and M2e3_E1_D8e26 (brown) simulations. The drop in the median value at $\approx$1.75 $t_{\rm ff}$ is due to a numerical error in setting the lower cutoff; however, since this occurs after the cloud has collapsed and the CRs have lost most of their energy it does not affect our results. Right: total gas mass as a function of the gas density and CR diffusion coefficient $D_{\rm sc}$ (not including resolved streaming, Section 2.2.6) for the M2e3_E1_DVAR simulation at $t = 0.5\ t_{\rm ff}$.

energy density declines over time in both the M2e3_E10_D8e25 and M2e3_E1_D8e25 clouds, the CR distribution is more variable throughout the M2e3_E10_D8e25 cloud. Figure 9 shows that the typical cloud gas in the M2e3_E1_D8e25 and M2e3_E10_D8e25 simulations has a characteristic ionization rate of $\zeta \approx 10^{-19}\,{\rm s}^{-1}$ and $2 \times 10^{-18}\,{\rm s}^{-1}$, respectively, relatively independent of gas density. The blue line indicates that the M2e3_E1_D8e25 cloud is strongly peaked at this value, especially at $n \gtrsim 10^4\,{\rm cm}^{-3}$. In contrast, the M2e3_E10_D8e25 cloud has an average CRIR between $\approx 10^{-18}$and $10^{-17}\,{\rm s}^{-1}$ depending on gas density, indicating that the distribution is not strongly peaked and has a range of values above and below the median CRIR. There are regions with $\zeta \gtrsim 10^{-17}\,{\rm s}^{-1}$ at all gas densities.

Figure 10 shows a phase plot of the ionization fraction for all runs at $t = 1.5 t_{\rm ff}$. We compute the ionization fraction following the convention used in GIZMO from the electron fraction $f_e$, neutral hydrogen fraction $f_{\rm H}$, and H II fraction $f_{\rm H\,II}$ as MAX($f_e$, $(1 - f_{\rm H})$, $f_{\rm H\,II}$). At this time, ionization produced by stellar feedback is still minimal, so the degree of ionization reflects the local CR energy density. The pale yellow line in the M2e3_noCRT panel shows the contribution assuming a fixed CRIR of $1.6 \times 10^{-17}\,{\rm s}^{-1}$, which is used in the M2e3_noCRT simulation. The dark patches in the upper left are produced by ionization caused by radiative feedback, while the area in the lower left shows the contribution from CR ionization. Since the CRIR is low for most of the runs, the contribution from CRs to the overall gas ionization is minor compared to the ionization caused by radiative feedback once star formation is underway.

## 4. Discussion

### 4.1. Propagation of CRs in Molecular Clouds

In this section, we discuss the implications of our results for the propagation of CRs within MCs.

#### 4.1.1. Role of the CR-driven Streaming Instability

We find that for all of the simulations except the M2e3_E1_D8e26 simulation, the CR energy density in the cloud is significantly lower than it is outside the cloud. The CR energy density in the cloud declines quickly as the cloud collapses and is not replenished by CRs from outside the cloud. To understand this result, we consider the relevant timescales for CR propagation and compare them to the loss timescales. The following expressions describe the timescale for each transport mechanism to propagate CRs a distance $L$ (e.g., Habegger et al. 2023):

$$\tau_{\rm adv} = L/v_{\rm adv} \approx 1 L_{\rm pc} v_{\rm km}^{-1} {\rm Myr}, \tag{18}$$

$$\tau_{\rm str} = L/v_{\rm st} \approx 1 L_{\rm pc} B_{\mu}^{-1} \rho_{-21}^{1/2} f_{-7}^{1/2}\,{\rm kyr}, \tag{19}$$

$$\tau_{\rm diff} = L^2/D_{||} \approx 3 L_{\rm pc}^2 D_{26}^{-1} {\rm kyr}, \tag{20}$$

for advection, streaming, and diffusion, respectively, where we assume $v_{\rm adv} = |\boldsymbol{u}|$ (the gas velocity), $v_{\rm st} = v_{\rm Ai}$, $L_{\rm pc}$, $v_{\rm km}$, $B_{\mu}$, $\rho_{-21}$, $f_{-7}$, and $D_{26}$ are the length scale, advection velocity, rms magnetic field, gas density, ionization fraction, and diffusion coefficient in units of 1 pc, $1\,{\rm km\,s}^{-1}$, $1\,\mu G$, $10^{-21}\,{\rm g\,cm}^{-3}$, $10^{-7}$, and $10^{26}\,{\rm cm}^2\,{\rm s}^{-1}$, respectively.

While they propagate, the CRs lose energy through streaming and collisional losses. If the amount of time for CRs to lose their energy through either one of these mechanisms is considerably shorter than the time for the CRs to propagate through the cloud, then the CRs will quickly lose energy, and thus the CR energy density will be low inside the cloud. The energy loss timescale from collisions is obtained from Equation (9):

$$\tau_{\rm cat,loss} = \Lambda_{\rm cr}^{-1} = (7.51 \times 10^{-16})^{-1} \left(\frac{n_H}{\rm cm^{-3}}\right)^{-1} {\rm s}. \tag{21}$$

The streaming loss term is calculated consistently in the simulations as $\Gamma_{\rm st} = -(\bar{v}_s/c^2) v_{\rm st} F_{e,{\rm cr}}$, where $\Gamma_{\rm st} = \Lambda_{\rm st} e_{\rm cr}$ and $\Lambda_{\rm st}$ is the streaming energy loss rate. The streaming loss timescale can be approximated as (Chan et al. 2019):

$$\tau_{\rm str,loss} = \Lambda_{\rm st}^{-1} = \left(\frac{1}{\gamma_{\rm cr} - 1}\right) |\hat{B} \cdot \hat{\nabla} \epsilon_{\rm cr}|^{-2} \left(\frac{\ell_{\rm cr}}{v_{\rm st}}\right) {\rm s}, \tag{22}$$

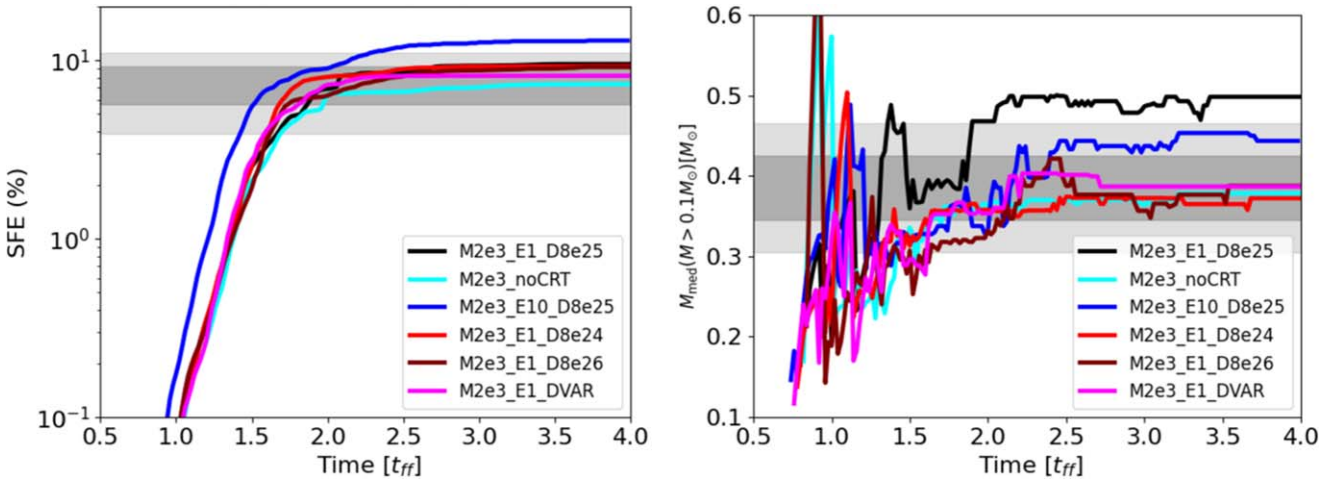


**Figure 7.** Left: evolution of the SFE vs. time for all simulations. Shaded regions are the $1\sigma$ (dark gray) and $2\sigma$ (light gray) final SFE values obtained from a set of 100 $2000M_\odot$ cloud simulations without CRT that vary the initial turbulent seed. Right: median mass for $M_* \geqslant 0.1M_\odot$ vs. time for all runs. Shaded regions are the $1\sigma$ (dark gray) and $2\sigma$ (light gray) final $M_{\rm med}$ values obtained from a set of previous simulations run without CRT, varying the initial turbulent seed.

**Table 3**
Final Values for the SFE, Median Mass Above the Incompleteness Region, and Maximum Mass for All Simulations at $4t_{\rm ff}$

| Simulation Name | SFE (%) | $M_{\rm med}(M > 0.1M_\odot)$ | $M_{\rm max}$ |
|---|---|---|---|
| M2e3_E1_D8e25 | 9.53 | 0.50 | 29.3 |
| M2e3_noCRT | 7.35 | 0.38 | 30.6 |
| M2e3_E10_D8e25 | 12.90 | 0.44 | 22.5 |
| M2e3_E1_D8e24 | 9.30 | 0.37 | 23.3 |
| M2e3_E1_D8e26 | 9.17 | 0.38 | 22.7 |
| M2e3_E1_DVAR | 8.19 | 0.39 | 19.1 |

where $\hat{\nabla}\epsilon_{\rm cr}$ is the unit vector of the CR energy density gradient $\nabla\epsilon_{\rm cr}$ and $\ell_{\rm cr} = \epsilon_{\rm cr}/\nabla\epsilon_{\rm cr}$ is the CR gradient scale length.

The advection timescale (Equation (18)) reflects the speed of the nonrelativistic gas and thus represents the gas crossing time in the simulation. Since our simulations use a comoving Lagrangian frame that moves with the gas, it is independent of the choice of $\tilde{c}$. The four other timescales ($\tau_{\rm str}$, $\tau_{\rm diff}$, $\tau_{\rm cat,loss}$, and $\tau_{\rm str,loss}$), however, represent CR propagation and losses away from the gas and thus these timescales are a factor $\Gamma_{\rm RSOL} = c/\tilde{c}$ slower due to the RSOL approximation (Hopkins et al. 2022b). For our value of $\tilde{c} = 300\,{\rm km\,s^{-1}}$, $\Gamma_{\rm RSOL} = 1000$. This caveat does not influence the conclusions of this section because we are concerned with the relative importance of these timescales and all of the timescales scale proportionally. We discuss the implications of the choice of $\tilde{c}$ further in Section 4.3 and in Appendix A.

Figure 11 (bottom) shows the five timescales as a function of the gas density for the M2e3_E1_D8e25 (solid), and M2e3_E1_D8e26 (dashed) simulations at $0.5\,t_{\rm ff}$, where the relevant gas quantities used to calculate the transport and loss timescales are displayed in the top panel. To reflect the behavior of the simulations we scale all timescales except for $\tau_{\rm adv}$ by a factor of $\Gamma_{\rm RSOL}$. For the M2e3_E1_D8e25 simulation transport due to streaming dominates over advective and diffusive transport throughout the cloud. This is especially true at the highest densities ($n \gtrsim 100\,{\rm cm^{-3}}$), where the ionization fraction is $f_{\rm ion} < 10^{-7}$, resulting in $v_{\rm Ai} > 1000\,{\rm km\,s^{-1}}$. The high streaming velocity also produces efficient energy losses from the streaming instability. Streaming losses dominate for gas densities $n < 10^4\,{\rm cm^{-3}}$ and collisional energy losses dominate at higher densities. Although the magnitudes of the transport and loss timescales vary with the CR and gas properties, all simulations except the M2e3_E1_D8e26 simulation have significant streaming instability energy losses, which cause the CRs to lose a significant amount of energy before propagating far in the cloud. To provide additional evidence for this result, we run low-resolution tests where we disable collisional losses and streaming transport and losses separately (see Appendix B).

The diffusive transport timescale is inversely proportional to the CR diffusion coefficient. For the M2e3_E1_D8e26 simulation, diffusive transport is comparable to streaming transport. Physically, the CRs scatter less and so effectively propagate more efficiently. The streaming timescale is also slightly higher due to the higher ionization fraction from the higher CR energy density in the cloud. Finally and most significantly, the streaming loss timescale is larger for the M2e3_E1_D8e26 simulation because the CR distribution is more uniform. The cumulative effect is that in the M2e3_E1_D8e26 simulation, CRs are able to propagate through the cloud without losing a significant amount of energy.

Our simulations show that streaming instability energy losses dominate over collisional losses for ∼GeV CRs, which has important physical and observational implications. The CR energy lost to the streaming instability goes into exciting Alfvèn waves, which are quickly damped by ion-neutral collisions that thermalize the energy. This means that the CR streaming instability provides a stronger source of gas heating than CR ionization. Furthermore, the CR energy is not lost to $\gamma$-ray production, especially not at the cloud boundary where streaming instability energy losses are strongest. This supports $\gamma$-ray observations from MCs that are in agreement with the solar neighborhood CRIR of $\zeta \approx 10^{-17}\,{\rm s^{-1}}$ (Krumholz et al. 2023) even though line-width observations suggest they have elevated CRIRs by approximately an order of magnitude (Indriolo et al. 2015). In other words, our simulations support the conclusion that the high CRIR values observed in Milky Way MCs do not come from an elevated *total* CR background. Instead, they may result from additional sources of low-energy ionizing CRs (∼MeV), which we discuss more in Section 4.2.1.

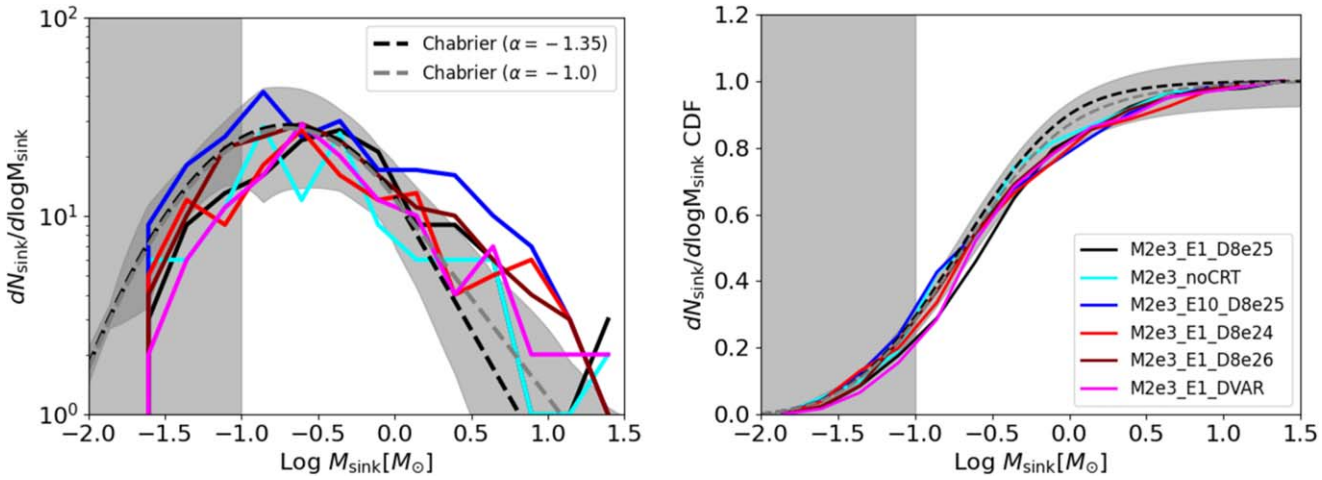


**Figure 8.** Left: stellar IMF for all runs at $t = 4t_{ff}$. The shaded region at $M < 0.1M_\odot$ indicates the low-mass incompleteness region (Grudić et al. 2021). Dashed lines show the Chabrier IMF (Chabrier 2005) with the standard slope of $\alpha = -1.35$ (black) and the slope obtained from previous STARFORGE simulations, $\alpha = -1$ (gray; Grudić et al. 2022; Guszejnov et al. 2022). The shaded region shows the $1\sigma$ values in each mass bin obtained from a set of 100 $2000M_\odot$ cloud simulations without CRT. Right: normalized cumulative distribution function of the IMF for all simulations.

On the other hand, $\gamma$-ray measurements from starburst galaxies indicate that they are proton-calorimeters, with all of their CR energy lost to catastrophic collisions. Our results suggest that in these galaxies the streaming speeds in MCs must be slower than in a Milky Way environment because otherwise, the CRs lose all of their energy to streaming losses. The ionization fraction is higher on average in starbursts than in Milky Way–type galaxies, with typical values from $\chi \approx 10^{-7}$–$10^{-4}$ (Krumholz et al. 2020). In regions of higher ionization the ion Alfvèn speed is lower and so the CRs can get "trapped" and lose their energy to hadronic losses rather than streaming losses.

#### 4.1.2. Exclusion of CRs from Molecular Clouds

Section 4.1.1 discusses how streaming instability energy losses cause the CRs initialized in the cloud to quickly lose energy once the cloud starts collapsing. However, this does not explain why CRs from outside the cloud do not propagate into the cloud and offset the energy losses. In this section, we discuss the effects that may be producing this "exclusion" of CRs from MCs, which has been noted in many previous studies (Kulsrud & Pearce 1969; Skilling & Strong 1976; Cesarsky & Volk 1978; Chandran 2000; Padoan & Scalo 2005; Everett & Zweibel 2011; Padovani & Galli 2011; Padovani et al. 2013; Silsbee et al. 2018; Bustard & Zweibel 2021).

The primary effect keeping CRs from propagating into the cloud is that streaming energy losses are even stronger at the cloud boundary than inside the cloud. Figure 11 shows that at $0.5t_{ff}$ the streaming loss timescale of the M2e3_E1_D8e25 simulation drops sharply at the outer cloud boundary region ($n \sim 1$–$10\,\mathrm{cm}^{-3}$) and reaches a minimum at the inner cloud boundary region ($n \sim 10$–$100\,\mathrm{cm}^{-3}$) because of the sharp gradient in the CR energy density. This indicates that CRs lose a significant amount of energy as they propagate through the boundary and into the cloud. We emphasize that this outcome is not due to the fact that we started the simulations with $\epsilon_{cr,cloud} = 0.1\epsilon_{cr,med}$, and it occurs even in tests beginning with $\epsilon_{cr,cloud} = \epsilon_{cr,med}$. Rather, the gradient in the CR energy density always develops at the cloud boundary because of the drop in the ionization fraction and the resulting increase in the ion Alfvèn velocity there (Figure 11).

The degree of CR exclusion from the cloud interior also depends on the diffusion coefficient. Across the entire cloud boundary region ($n \sim 1$–$100\,\mathrm{cm}^{-3}$), the diffusive transport timescale is comparable to that of streaming transport. Physically, the CRs have a longer path length in the M2e3_E1_D8e26 simulation, and gradients in the CR energy density are wiped out faster. For the M2e3_E1_D8e26 simulation, the streaming loss timescale is roughly uniform across the cloud boundary, because no sharp gradients in the CR energy density develop.

The CR exclusion at the cloud boundary may also be enhanced by magnetic field effects. Figure 12 shows slices of the gas density (top), CR energy density (middle), and rms magnetic field $B_{rms}$ (bottom) at $0.5t_{ff}$ through the middle of the domain for the M2e3_E1_D8e25 (left), M2e3_noCRT (middle), and M2e3_E1_D8e26 (right) simulations. The magnetic field in the cloud is up to an order of magnitude higher than the magnetic field in the ambient medium, setting up a strong magnetic gradient. However, the magnetic field behavior at the cloud boundary is complex: there is a region with a slightly elevated magnetic field that is a few $\mu$G higher than the medium value at $n \sim 1\,\mathrm{cm}^{-3}$, followed by a pocket of low-magnetic field that coincides with the boundary region ($n \sim 1$–$100\,\mathrm{cm}^{-3}$). This magnetic behavior is similar in all three simulations and coincides with the phase transition from ionized to neutral gas. In the simulations with CRT, the highly magnetized ring aligns with a peak in the CR energy density (shown by the yellow rim). In the M2e3_E1_D8e26 simulation, a ring of enhanced CR energy density is faintly visible, but the CR distribution is mostly uniform throughout the cloud and medium. The CRs have a longer path length in the M2e3_E1_D8e26 simulation, which allows them to more easily scatter over magnetic field asymmetries into the cloud.

We note that in our simulations this "ring" effect may be due to the initialization of the CR energy and the varying cell size across the cloud boundary. If the CRs were able to diffuse freely in this region then the excess may be rapidly smoothed out; instead, the enhancement persists even in the M2e3_E1_D8e26 simulation. Still, the spatial correlation between the CRs and the magnetic field deserves consideration due to the number of studies that have looked at the effects of

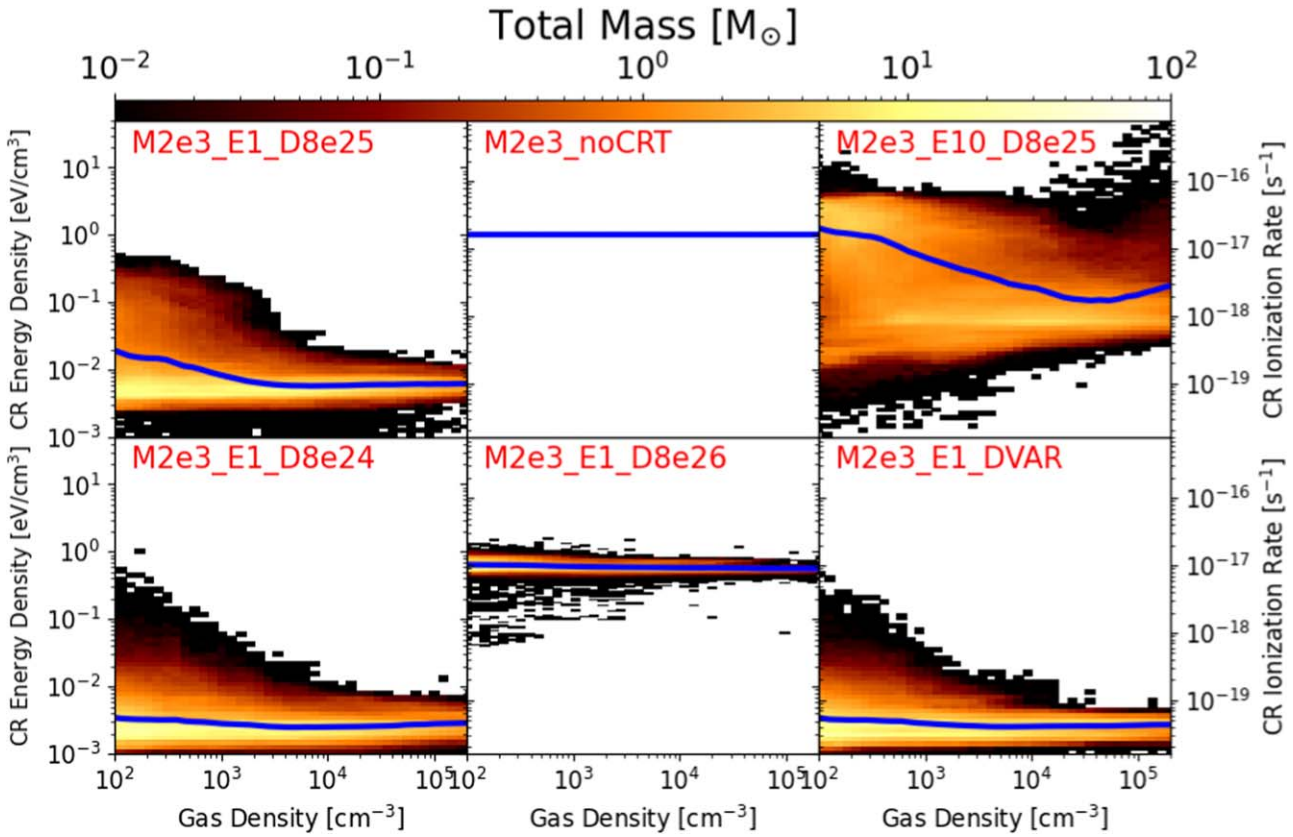


**Figure 9.** Total mass of cells as a function of the gas density and CR energy density for all simulations at $t = 1.5\ t_{\rm ff}(\approx 3$ Myr). The blue line shows the mass-weighted mean CR energy density at each gas density. On the right hand is the corresponding CR ionization rate. The horizontal blue line in the M2e3_noCRT panel is the MW CR energy density ($\epsilon_{\rm cr} = 1$ eV cm$^{-3}$) assumed when CRT is not used.

large-scale nonuniformity of the magnetic field on CR propagation. Magnetic field lines converge in regions undergoing gravitational collapse which results in a proportional increase in the number density of CRs, a phenomenon known as "focusing". On the other hand, the CRs' pitch angles increase in response to the growing field, and more particles are reflected back, known as "mirroring." A variety of studies have investigated the competing effects of magnetic mirroring and focusing on CR propagation in MCs (Kulsrud & Pearce 1969; Skilling & Strong 1976; Cesarsky & Volk 1978; Chandran 2000; Padoan & Scalo 2005; Silsbee et al. 2018) and in dense cores (Padovani & Galli 2011; Padovani et al. 2013; Fatuzzo & Adams 2014). Which effect dominates depends on the assumed magnetic geometry and details of the CR microphysics.

Recent studies have suggested that although magnetic fields may partially screen CRs from MCs, the effect is at most modest. Padovani & Galli 2011 and Padovani et al. (2013) find that mirroring dominates over focusing for dense cores but only causes a reduction in the CR energy density by a factor of 2–3 compared to the case where these effects are neglected. Silsbee et al. (2018) found that the two effects cancel except in magnetic "pockets," local minima in the field strength, where mirroring again dominates by trapping CRs in the pocket; however, even in these regions the reduction in the CRIR is less than an order of magnitude. We conclude that although the CR enhancement along the magnetic field gradient at the boundary may be physical rather than numerical, the primary effect excluding CRs from the cloud interior is streaming instability energy losses.

Past numerical studies have identified CR exclusion from MCs; however, most of them have attributed the cause to effects other than streaming losses. Skilling & Strong (1976) and Cesarsky & Volk (1978) found a drop in CR energy density for CRs of $E < 300$ MeV due to ionization losses, thereby creating a CR gradient that amplified the streaming instability at the boundaries of clouds. Although we have a gradient in the CR energy density at the cloud boundary due to the streaming instability, our single-bin approximation of CRs approximates ∼GeV CRs which do not experience the strong ionization losses present in ∼MeV CRs, so this effect is not present here.

Our findings are consistent with a few prior studies. Everett & Zweibel (2011) considered a similar simulation configuration in which ionization losses are also subdominant to streaming losses. They showed that even a small CR pressure gradient amplifies the growth of the CR streaming instability. However, they found only a small drop in CRs at the boundaries of clouds rather than the almost complete exclusion we found. Bustard & Zweibel (2021) considered more complex cloud geometries and a more advanced CRT model. Their results show gradients in the CR energy density at the cloud boundary similar to those in our simulations.

Most prior studies (Kulsrud & Pearce 1969; Skilling & Strong 1976; Cesarsky & Volk 1978; Chandran 2000; Padoan & Scalo 2005; Padovani & Galli 2011; Padovani et al. 2013; Silsbee et al. 2018) solve a set of simplified CR propagation equations that model a steady-state, nearly isotropic CR distribution, and they do not model the evolution of the gas and magnetic field. Even more importantly, they make the approximation that CR pitch-angle scattering due to the

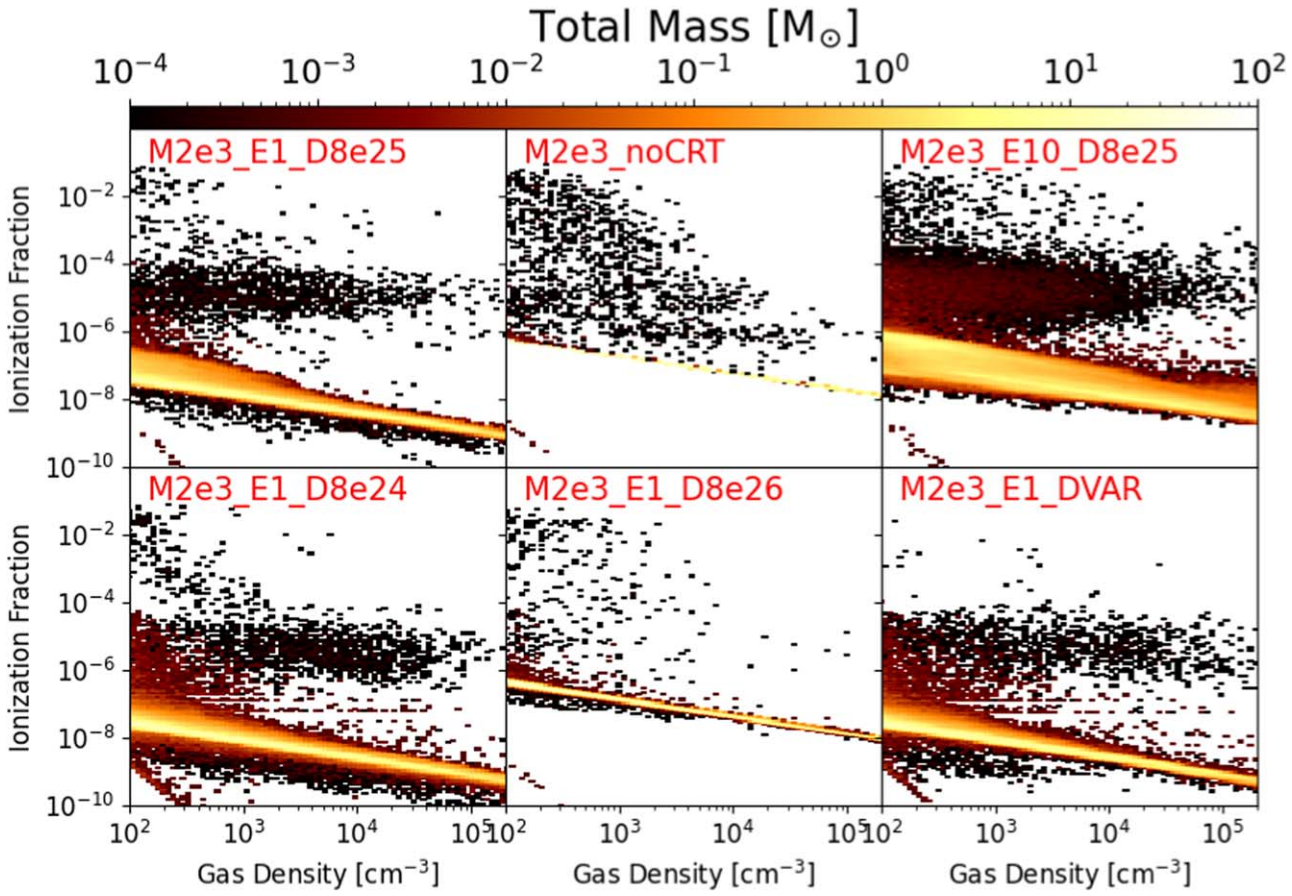


**Figure 10.** Total mass of cells as a function of the gas density and ionization fraction for all simulations at $t = 1.5\ t_{\rm ff}(\approx 3$ Myr). The yellow regions in each panel correspond to CR ionization, while the dark patches are from radiative feedback. The pale yellow line in the M2e3_noCRT panel shows the contribution assuming a fixed CRIR of $1.6 \times 10^{-17}$ eV cm$^{-3}$, which declines with gas density as $1/\sqrt{n_H}$. The descending line in all CRT simulations with ionization fraction $<1e-8$ and density $<1e3$ is due to a known bug in GIZMO where one particle per message passing interface (MPI) rank is assigned $\epsilon_{\rm cr} = 0$. Given the fact that we use $2 \times 10^6$ cells and only $\sim$200 MPI ranks, this bug impacts very few cells and thus does not have an effect on our results.

streaming instability is negligible and only model CR streaming along field lines. This is a reasonable assumption on microphysical timescales such as the CR gyro time or ion-neutral damping timescale, where streaming instability energy losses are insignificant (Kulsrud & Pearce 1969); however, on the longer timescales of MC evolution comparable to CR transport timescales, CRs are expected to lose a large fraction of their energy (Wentzel 1971). Everett & Zweibel (2011) and Bustard & Zweibel (2021) both model CRs interacting with diffuse clouds; thus, they use more advanced moment-based CRT models and consider $\sim$GeV CRs to more accurately capture streaming transport and scattering. However, Everett & Zweibel (2011) do not model the evolution of the cloud properties. Bustard & Zweibel (2021) provide the most accurate point of comparison to our simulations; however, their two-moment CRT implementation is only accurate for steady-state, close-to-isotropic cases. *None* of these studies considered the full effect of streaming energy losses on the further cloud evolution, which we have shown is an important component of CR physics that should be considered in future studies.

#### *4.1.3. Are Streaming Instability Energy Losses Unavoidable in Molecular Clouds?*

The results of our simulations suggest that streaming instability energy losses strongly limit the CR energy density in MCs. In this section, we discuss whether this is an unavoidable outcome of CR physics in MCs.

We first consider the situation where the CRT is streaming-dominated, which is the case in all except the M2e3_E1_D8e26 simulation. In this limit, the Eulerian equation for the CR energy density solved by many other studies (e.g., Chan et al. 2019) converges to $\partial \epsilon_{\rm cr}/\partial t = -\epsilon_{\rm cr} \nabla \cdot \boldsymbol{v}_{\rm st} - \gamma_{\rm cr} |v_{\rm st}| \epsilon_{\rm cr}/\ell_{\rm cr}$. This equation limits to $\epsilon_{\rm cr} \rightarrow 0$ if the streaming velocity increases going into the cloud ($\nabla \cdot \boldsymbol{v}_{\rm st}$ is positive) and/or $|\epsilon_{\rm cr} \nabla \cdot \boldsymbol{v}_{\rm st}| < |\gamma_{\rm cr} v_{\rm st} \epsilon_{\rm cr}/\ell_{\rm cr}|$. The only way for $\epsilon_{\rm cr}$ to stabilize at a higher value is if $|\epsilon_{\rm cr} \nabla \cdot \boldsymbol{v}_{\rm st}| > |\gamma_{\rm cr} v_{\rm st} \epsilon_{\rm cr}/\ell_{\rm cr}|$ and $v_{\rm st}$ decrease going into the cloud. However, this is the opposite of the expected behavior, because the ionization fraction decreases in the cloud, and the streaming velocity increases (Figure 11). Consequently, streaming losses are unavoidable if streaming is the dominant transport mechanism.

Next, we consider the case where streaming and diffusive transport are comparable as in our M2e3_E1_D8e26 simulation. This simulation models an environment with a strong macroscopic diffusivity $D_{\parallel,\rm FLW}$ where turbulence advects the magnetic field lines at a rate faster than streaming energy losses remove energy. However, this scenario was only realized by ad-hoc setting the diffusion coefficient to a high value and is not consistent with the degree of field-line wandering expected in mostly neutral gas unless $f_{\rm ion} \lesssim 10^{-9}$ (Sampson et al. 2023). Figure 10 shows that an ionization fraction this low is rarely

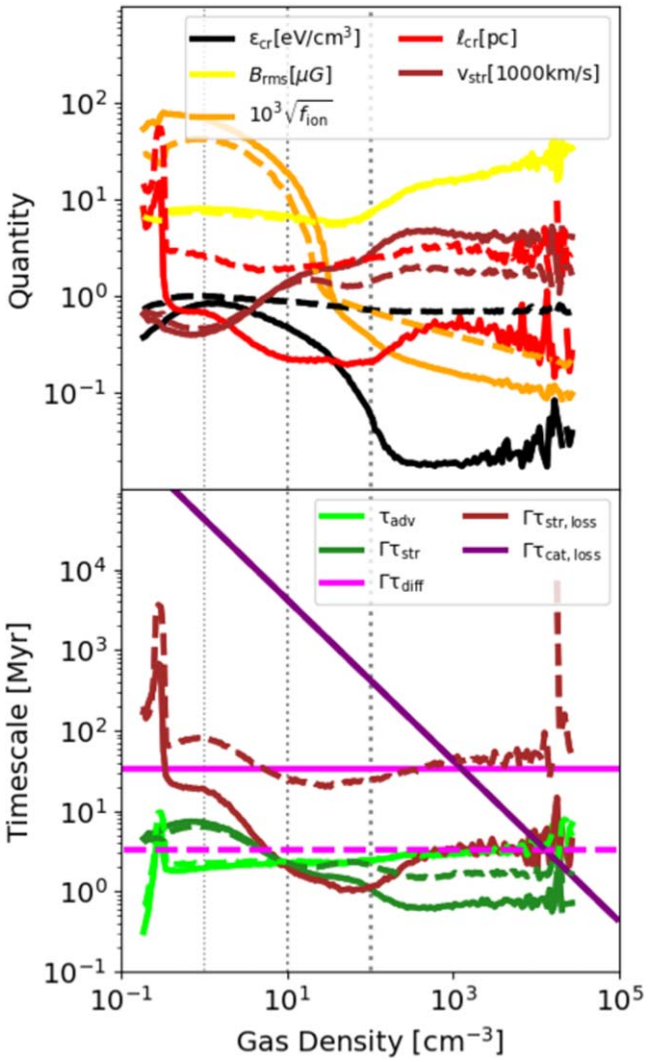


**Figure 11.** Top: median values of the CR energy density $\epsilon_{cr}$, rms magnetic field $B_{rms}$, ionization fraction $f_{ion}$, CR gradient scale length $\ell_{cr} = \epsilon_{cr}/\nabla\epsilon_{cr}$, and streaming velocity $v_{st}$ as a function of the density as used in the calculation of the streaming timescale $\tau_{str}$ (Equation (19)) and the streaming loss timescale $\tau_{str,loss}$ (Equation (22)) at $0.5t_{ff}$. The vertical gray dotted lines correspond to gas densities $n = 1,\ 10,\ 100\ \mathrm{cm^{-3}}$. Bottom: advection timescale $\tau_{adv}$, streaming timescale $\tau_{str}$, diffusion timescale $\tau_{diff}$, streaming loss timescale $\tau_{str,loss}$, and collisional loss timescale $\tau_{cat,loss}$ from Equations (18), (19), (20), (21), and (22), respectively, as a function of the gas density for the M2e3_E1_D8e25 (solid) and M2e3_E1_D8e26 (dashed) simulations at $0.5t_{ff}$. The transport timescales $\tau_{adv}$, $\tau_{str}$, and $\tau_{diff}$ assume a characteristic length scale of $L = 3$ pc. The values of the streaming timescales $\tau_{str}$ and $\tau_{str,loss}$, and the advection timescale $\tau_{adv}$ are calculated using the median values of gas and CR properties at each gas density. All timescales except $\tau_{adv}$ are scaled by $\Gamma_{RSOL} = c/\tilde{c}$. The vertical gray dotted lines correspond to gas densities $n = 1,\ 10,\ 100\ \mathrm{cm^{-3}}$.

achieved in our simulations, especially near the cloud boundary, and, furthermore, is not in line with measured values in MCs, (Caselli et al. 1998). Moreover, this limit could not be sustained because the CRs would stream with minimal energy losses, which would increase $f_{ion}$ and thereby decrease the ion Alfvén velocity.

It is also impossible to achieve this limit with microphysical diffusion. As discussed in Section 2.2.6, if the streaming instability is the only source of microphysical scattering then achieving $v_{diff} \gg v_{Ai}$ would require $\epsilon_{cr} \ll 1$ eV cm$^{-3}$. Adding additional sources of CR scattering from extrinsic turbulence would decrease $D_{\parallel,micro}$; in other words, assuming scattering due to self-generated turbulence alone provides an upper limit to $D_{\parallel,micro}$. Therefore, it is not possible to reach the diffusion-dominated transport limit unless $\epsilon_{cr} \ll 1$ eV cm$^{-3}$ in the cloud from the start.

An alternative way to reduce streaming losses is to suppress the growth of the streaming instability by limiting the drift velocity to less than the ion Alfvèn velocity ($v_D = v_{st} + v_{diff} < v_{Ai}$). In a steady state, the growth rate of the streaming instability (Equation (15)) is matched by the ion-neutral damping rate (Equation (14)), which sets the diffusive component of the velocity $v_{diff}$. However, Equation (15) shows that when $v_D < v_{Ai}$ and $\Gamma_{SI} < 0$, the streaming instability will never grow. In our simulations, we directly model CR streaming using $v_{st} = v_{Ai}$ and include $v_{diff}$ using the diffusion coefficient $D_{\parallel}$, so by construction, we cannot capture a situation where $v_D < v_{Ai}$. However, in principle, the streaming velocity could be less than the ion Alfvèn velocity. One way to achieve this is if $v_{Ai} \gtrsim c/3$ (where the factor of 3 comes from appropriately including the moments of the CR distribution function). Using appropriate gas quantities ($B \sim 10\mu$G, $n \sim 100\,\mathrm{cm^{-3}}$, $\mathrm{m_{ion}} \sim 29\mathrm{m}_p$), $v_{Ai} \approx 0.5 f_{ion}^{-1/2}$ km/s and so achieving $v_{Ai} \gtrsim c/3$ would require $f_{ion} \lesssim 10^{-9}$. For the reasons discussed above, this limit could not be sustained.

Another way to keep $v_D < v_{Ai}$ is through an extrinsic source of strong, symmetric scattering modes that scatter the CRs isotropically. The full expression for the CR streaming speed is $v_{st} = v_{Ai}(\bar{\nu}_s^+ - \bar{\nu}_s^-)/(\bar{\nu}_s^+ + \bar{\nu}_s^-)$, where $\bar{\nu}_s^+$ and $\bar{\nu}_s^-$ are the scattering modes for forward and backward propagating waves, respectively (Hopkins et al. 2021a). Extrinsic sources of turbulence tend to produce symmetric scattering with $\bar{\nu}_s^+ \approx \bar{\nu}_s^-$. In this limit, $v_{st} \to 0$ so the $v_{st}$ terms in Equations (4) and (5) vanish, and the diffusive acceleration term $\tilde{S}_{sc}$ dominates, meaning the CRs may gain energy as they propagate.

For this model to be viable, the turbulence must be strong enough such that $v_{diff} \sim D_{\parallel,micro}/\ell_{cr} \ll v_{Ai}$ so the streaming instability is not excited in the first place. Using appropriate quantities for the diffuse ISM ($B \sim \mu G$, $n \sim 1\,\mathrm{cm^{-3}}$, $\mathrm{m_{ion}} \sim \mathrm{m}_p$), $v_{Ai} \approx 2\,\mathrm{km/s}\ f_{ion}^{-1/2}$, and so $D_{\parallel} \lesssim 5 \times 10^{23} (\ell_{cr}/\mathrm{pc}) \mathrm{f_{ion}^{-1/2}} \mathrm{cm^2 s^{-1}}$. This value is much lower than the microphysical diffusivity in the diffuse ionized ISM ($f_{ion} \approx 1$), where simulations estimate the diffusivity at a few $\times 10^{28}\,\mathrm{cm^2\,s^{-1}}$ (Trotta et al. 2011). Moreover, this scattering would have to be strong enough to compete with ion-neutral damping in MCs. We tested this scenario by including a standard model for extrinsic turbulence scattering in our M2e3_E1_DVAR simulation and found that this limit was never reached (otherwise, there would have been no streaming transport or losses in that simulation).

We conclude that any scenario in which streaming instability energy losses are avoided in MCs requires new physics. Either our understanding of the CR streaming instability and self-confinement is wrong, or there are sources of extrinsic turbulence that are stronger than any currently known that can produce the necessary scattering.

### 4.2. Comparison to Observations

#### 4.2.1. Ionization Within Molecular Clouds

Measured values of the CRIR in the Milky Way vary by over an order of magnitude. The value measured directly by the Voyager spacecraft, which has the lowest amount of uncertainty, is $\zeta \sim 2 \times 10^{-17}\,\mathrm{s^{-1}}$ (Stone et al. 2019). However, this only probes the CRIR in the Solar neighborhood. Indirect

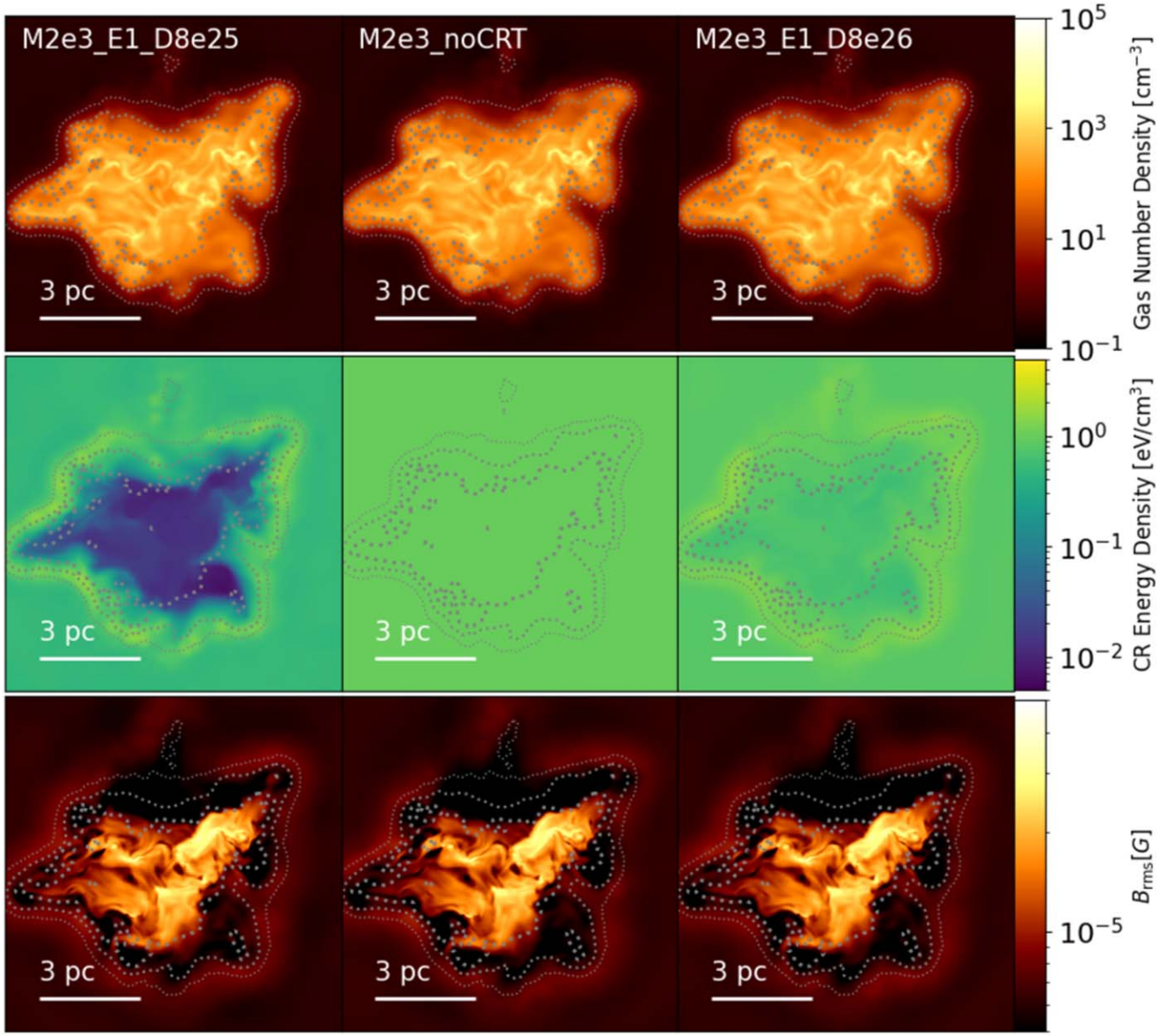


**Figure 12.** Gas number density (top), CR energy density (middle), and rms magnetic field (bottom) for the M2e3_E1_D8e25 (left), M2e3_noCRT (middle), and M2e3_E1_D8e26 (right) simulations at $0.5t_{ff}$. For the M2e3_noCRT panel, a CR energy density of $\epsilon_{cr} = 1$ eV cm$^{-3}$ is shown, corresponding to the assumed ionization rate of $\zeta \sim 1.7 \times 10^{-17}$s$^{-1}$. The gray dotted contours correspond to gas densities $n = 1$, 10, 100 cm$^{-3}$, also marked in Figure 11.

measurements of the CRIR obtained from $H_3^+$ observations of diffuse molecular gas suggest the CRIR varies over a few orders of magnitude within the Milky Way, with an average value of a few $\times 10^{-16}$ s$^{-1}$ (Indriolo & McCall 2012; Indriolo et al. 2015; Neufeld & Wolfire 2017; Kálosi et al. 2023).

Although most of our simulations assume a CR background consistent with that measured by Voyager, only the M2e3_E1_D8e26 simulation reached a CR level throughout the cloud of $\zeta \sim 10^{-17}$. Our M2e3_E10_D8e25 simulation, which adopted an external CR energy density 10 times that measured by Voyager, had a larger range of CRIRs throughout the cloud than the other simulations (top right panel of Figure 9). However, it still had a significantly lower CR energy density inside the cloud due to CR exclusion. These results suggest that the observed elevated ionization rates are unlikely to come from spatial variations in the galactic CR distribution pervading the clouds. For low to moderate values of the CR diffusion coefficient, the CRs lose a significant amount of energy due to the streaming instability. For high values of the CR diffusion coefficient, the CRs do not scatter enough to create significant spatial variations.

Measurements of higher-density gas tracers indicate that there is tentative evidence that the CRIR declines in higher-column-density gas (e.g., Padovani 2023). Ionization maps of dense MCs using $H_2D^+$ show CRIRs lower than those in diffuse clouds ranging from a few $\times 10^{-17}$–$10^{-16}$ s$^{-1}$, in agreement with this conclusion (Sabatini et al. 2023). However, they also show that within MCs the CRIR often spans orders of magnitude as well. Observations of $HCO^+$ and $N_2H^+$ along sight lines toward the intermediate-mass protostar OMC-2 FIR 4 indicate values of $\approx 10^{-14}$ s$^{-1}$, a couple orders of magnitude *higher* than the mean CRIR (Ceccarelli et al. 2014; Fontani et al. 2017). Meanwhile, ionization maps of the Class 0 protostar B335 show large fractions of ionized gas

($f_{\rm ion} \approx 1 - 8 \times 10^{-6}$) and suggest the ionization increases toward small envelope radii, reaching values of $\sim 10^{-14}\,{\rm s}^{-1}$ a few hundred astronomical units from the central protostar (Cabedo et al. 2023).

Models used to derive the CRIR using dense gas tracers have significant uncertainties and their accuracy varies with the source properties (Shingledecker et al. 2016). Still, none of our simulations produced regions approaching the elevated values inferred for B335. They show that streaming instability energy losses result in a uniform CRIR throughout the cloud, without enhancements in denser regions.

Our study lends support to the idea that there may be internal sources of CR acceleration within MCs associated with the protostellar shocks (Padovani et al. 2016; Gaches & Offner 2018; Fitz Axen et al. 2021). Krumholz et al. 2023 estimate that protostellar sources contribute $\sim 1/4$–$1/3$ as much energy to the galactic CR energy budget as stellar winds. Low-mass stars form earlier and are more numerous than high-mass stars, and so would accelerate CRs earlier in the cloud collapse than stellar winds. These CRs may explain the observed high CRIRs, especially near protostars, as well as the overall elevated ionization rates inferred in diffuse clouds. However, the degree of ionization inside clouds is sensitive to CR physics and the CR diffusion coefficient, which is highly uncertain. Thus, ionization rate measurements and comparisons based on synthetic observations can provide helpful constraints for models of CR acceleration and propagation within MCs.

#### 4.2.2. Star Formation in a High-CR environment

Many regions in the Milky Way and other galaxies have a CRIR that is higher than the Voyager value of $\sim 10^{-17}\,{\rm s}^{-1}$. In particular, recent observations show evidence of elevated CRIRs toward the center of galaxies. Although the Galactic average is $\approx 2 \times 10^{-16}\,{\rm s}^{-1}$ (Indriolo et al. 2015), the CRIR measured in the central parsec of the Milky Way is $\approx$2 orders of magnitude higher than that in the clouds outside the galactic center (Goto 2014; Indriolo et al. 2015; Rivilla et al. 2022). Extragalactic measurements toward the central molecular zone of the starburst galaxy NGC 253 suggest even higher values. Holdship et al. (2022) studied several star-forming regions there and found CRIR values between $1 - 80 \times 10^{-14}\,{\rm s}^{-1}$. Behrens et al. (2022) found that the central GMCs of NGC 253 had $\zeta \approx 10^{-13}$–$10^{-11}\,{\rm s}^{-1}$, greater than 4 orders of magnitude higher than the Milky Way value.

We note that the accuracy of these measurements is in tension with theoretical predictions. Krumholz et al. (2023) argue that these CRIR values are inconsistent with the measured star formation rates, which determine the amount of energy available for accelerating CRs, and that the true CRIRs are significantly lower, though still likely a factor of 10–100 greater than the Voyager value. They are also inconsistent with other observational and theoretical expectations, which predict an anticorrelation between CRIR and gas density (Indriolo & McCall 2012; Neufeld & Wolfire 2017; Padovani 2023). However, regions of the ISM near SNRs may have elevated CR levels, as SNRs are thought to be the primary accelerators of Galactic CRs (Aharonian 2013). Indeed, measurements of CRIRs targeting clouds near SNRs show elevated rates of $\approx$100 times the Galactic average (Ceccarelli et al. 2011; Vaupré et al. 2014).

We found that star formation occurs more rapidly and the SFE is a few percent higher in our M2e3_E10_D8e25 simulation, which raises the CR background level by only an order of magnitude. Thus, we might expect larger differences in star formation in even more extreme CR environments, such as near SNRs. However, the details of the effect are highly sensitive to the assumed value of the diffusion coefficient. Raising the diffusion coefficient by an order of magnitude caused a large difference in the CR propagation within the cloud, diminishing energy losses from the streaming instability and exclusion by magnetic fields. Meanwhile, decreasing the diffusion coefficient by an order of magnitude caused even more rapid CR energy losses. These results suggest a higher diffusion coefficient and a higher CR environment acting in concert could produce more extreme variations in star formation outcomes. Further work is needed to investigate this parameter space.

### 4.3. Simulation Caveats

#### 4.3.1. Energy–independent Treatment of CRs

Our simulations make a number of approximations in the treatment of CR physics. We use a single-bin model for the CR fluid that represents the total CR energy rather than evolving a full multibin energy spectrum. The treatment of the CR velocities and the energy loss function assume $\sim$GeV CRs. Simulations modeling a full multibin CR energy spectrum that extends down to $\sim$MeV and up to $\sim$TeV energies would likely predict different CR behavior within the dense gas. For example, $\sim$MeV CRs more efficiently ionize gas than $\sim$GeV CRs. Collisional energy losses are anticorrelated with the gas density (see Equation (9)), so multibin CRT simulations might better reproduce the apparent density-dependent CRIR seen in observations (Padovani 2023). Modeling CRs with $\gtrsim$ GeV energies would likely have a minimal impact on our results because these CRs are less numerous than CRs of lower energies (Stone et al. 2019). However, these CRs produce $\gamma$-rays, so comparisons to observed $\gamma$-ray emission could lead to additional constraints on CRT in MCs.

We note that modeling a full CR spectrum would not change the conclusions presented in Section 4.1.3 because they apply at all CR energies as long as the streaming instability dominates the CR scattering. CRs of all energies will stream at the ion Alfvèn speed and experience streaming energy losses. Thus, the cloud will still develop a low CR energy density eventually, even if there is measurable ionization and $\gamma$ ray emission before the CRs lose their energy.

#### 4.3.2. RSOL Approximation

We use an RSOL of $300\,{\rm km\,s}^{-1}$ for our simulations to make them computationally tractable. This is higher than the value used for other STARFORGE calculations of $\tilde{c} = 30\,{\rm km\,s}^{-1}$ (Grudić et al. 2021, 2022) or $\tilde{c} = 90\,{\rm km\,s}^{-1}$ (Grudić et al. 2023), which has been thoroughly tested for non-CRT simulations in which the RSOL affects the radiative transfer calculation. The choice of RSOL should not have a significant impact on our results as long as it is higher than the other relevant velocities in the simulations such as the CR streaming speed $v_{\rm st}$ and the diffusion speed set by the diffusivity $D_{\parallel}$. Otherwise, the CR transport and loss processes may be artificially slowed down (Hopkins et al. 2020). As discussed in Section 4.1.1 and shown in Figure 12, the streaming velocity is an order of magnitude higher than $300\,{\rm km\,s}^{-1}$ in many regions of the cloud. In order to justify our choice of RSOL, we run a

suite of low-resolution simulations that vary the RSOL. We find that using a higher RSOL increases the speed of CR transport and the rate of CR energy losses in the cloud but does not significantly affect the star formation properties. We show these results and discuss the implications further in Appendix A.

#### 4.3.3. Subgrid Models and Resolution

Our simulations predict an IMF with a high-mass slope $\alpha = -1$ consistent with results from previous STARFORGE calculations (Figure 8). As discussed in Grudić et al. (2022), limitations due to the feedback models and resolution may produce a shallower IMF than the commonly assumed value of $\alpha = -1.35$.

The STARFORGE protostellar jet feedback model, discussed in Section 2.1.1, uses fixed parameters $f_w = f_K = 0.3$, which parameterize the jet velocities but are observationally uncertain (Cunningham et al. 2011). Variations in these parameters which increase the jet velocity may regulate massive star formation (Guszejnov et al. 2021; Rosen et al. 2021).

We are limited in resolution in both length scale and mass (Grudić et al. 2022; Guszejnov et al. 2022). Size scales smaller than the Jeans length are not well resolved in the simulations, so protostellar disks are unresolved. Disk fragmentation may affect the stellar multiplicity and mass ratio distribution of binaries (Offner et al. 2023), so fully resolving disks may steepen the IMF.

#### 4.3.4. Calculation of the Streaming Speed

To calculate the ion Alfvèn velocity, GIZMO assumes $m_{\rm ion} = m_p$, which is equivalent to setting $\chi = f_{\rm ion}$. This is not a correct assumption for MCs, where the dominant charge carrier is $HCO^+(m_{\rm ion} = 29 m_p)$, and so overestimates $v_{\rm Ai}$ by a factor of $\sim\sqrt{29} \approx 5$. Additionally, we do not account for the effect of dust damping on the CR streaming speed. Dust grains can dampen the amplitude of the Alfvèn waves from the streaming instability, reducing the scattering rate and increasing the streaming speed (Squire et al. 2021).

Since both streaming transport and losses scale with $v_{\rm Ai}$, these caveats do not change the major conclusions presented throughout Section 4 emphasizing the importance of streaming losses when the CR transport is dominated by streaming. However, they may modify when CRs are in the streaming versus diffusion-dominated regimes (Section 4.1.1). These uncertainties are comparable to others in the chemistry module, and for given values of $v_{\rm st}$ and $v_{\rm diff}$ our conclusions are robust.

## 5. Conclusions

In this work, we present numerical simulations of the collapse of MCs including CRT as part of the STARFORGE project. These simulations follow the formation of individual stars and include all major stellar feedback mechanisms including protostellar jets, radiation, and stellar winds. We expand on previous STARFORGE simulations by explicitly modeling CRT using a single-energy-bin model of CRs, which are evolved as a fluid using an M1-moment-based method. We explore variations in the initial CR energy density and CR diffusion model. Our main findings are as follows:

1. In a fiducial CR environment where $\epsilon_{\rm cr} = 1$ eV cm$^{-3}$, including CRT, does not produce a strong difference in the dynamics of the gas collapse compared to simulations without CRT (Figures 1 and 3). This is true regardless of the model used for the diffusion coefficient (Figure 5).
2. In a high-CR environment where $\epsilon_{\rm cr} = 10$ eV cm$^{-3}$, the enhanced CR pressure outside the cloud causes faster collapse, earlier star formation, and a higher final SFE (Figure 5). The SFE in the high-CR environment increases earlier due to the earlier cloud collapse but progresses at the same rate as clouds embedded in a typical CR environment.
3. For low to moderate values of the CR diffusion coefficient, streaming instability energy losses strongly attenuate the CRs (Figure 2). However, when the diffusion coefficient is high enough ($\gtrsim 10^{26}$ cm$^2$ s$^{-1}$) the CRs lose less energy and distribute uniformly throughout the cloud at a level similar to that outside the cloud (Figure 5).
4. In a CR environment where $\epsilon_{\rm cr} = 1$ eV cm$^{-3}$ the evolution of the SFE is insensitive to the CR treatment (Figure 7). The final SFE is slightly higher for all of the CRT clouds than for the cloud with no explicit CRT. The no-CRT simulation has SFE $\approx 7\%$, while all of the CRT simulations have SFE $= 8\%$–$10\%$. The high-CR cloud has an SFE $> 12\%$.
5. Variations in the CR diffusion coefficient do not have a statistically significant impact on the IMF of the clouds (Figure 8). All simulations in an environment with $\epsilon_{\rm cr} = 1$ eV cm$^{-3}$ have a final stellar mass distribution consistent with previous STARFORGE calculations, with a peak at $\sim 0.2$–$0.3 M_\odot$ and a high-mass slope of $\alpha \approx -1$. However, one of the CRT simulations (M2e3_E1_D8e25) has a higher median mass, possibly due to stellar wind CR feedback that changes the gas conditions inside the cloud. In a high-CR environment with $\epsilon_{\rm cr} = 10$ eV cm$^{-3}$ the cloud forms both more low-mass ($M < 0.1 M_\odot$) and high-mass ($M > 1 M_\odot$) stars.
6. In a fiducial CR environment the CRIR is roughly uniform throughout the cloud (Figure 9). For low to moderate values of the CR diffusion coefficient it is up to a few orders of magnitude less than outside the cloud, with a median value $\zeta \lesssim 2 \times 10^{-19}$ s$^{-1}$ at 1–1.5 $t_{\rm ff}$. In a high-CR environment simulation the CRIR in the cloud is higher than in a fiducial environment ($\zeta \lesssim 6 \times 10^{-18}$ s$^{-1}$) and there is a larger spread of values, but is still less than the commonly assumed value of $\sim 10^{-17}$ s$^{-1}$ throughout most of the cloud. Overall, the CR background does not provide a significant contribution to the ionization of the cloud compared to radiative feedback once star formation is underway (Figure 10).

Further numerical studies exploring the impact of a high CR diffusion coefficient in high-CR environments may provide further insights and constraints on CRT. Furthermore, numerical simulations including locally injected CRs from protostellar sources may explain the elevated CRIRs and variations within clouds observed from various sources.

## Acknowledgments

This research is part of the Frontera computing project at the Texas Advanced Computing Center and used computing award AST21002. Frontera is made possible by the National Science Foundation award OAC-1818253. This research was supported in part by NASA ATP grant 80NSSC20K0507. This material is based upon work supported by the U.S. Department of Energy, Office of Science, Office of Advanced Scientific Computing Research, Department of Energy Computational Science Graduate Fellowship under Award No. DE-SC0021110. Support for P.F.H. was provided by NSF Research Grants

1911233, 20009234, 2108318, NSF CAREER grant 1455342, NASA grants 80NSSC18K0562, HST-AR-15800. M.R.K. acknowledges support from the Australian Research Council with the *Discovery Projects* and *Laureate Fellowship* schemes, awards DP 230101055 and FL220100020. Support for M.Y.G. was provided by NASA through the NASA Hubble Fellowship grant #HST-HF2-51479 awarded by the Space Telescope Science Institute, which is operated by the Association of Universities for Research in Astronomy, Inc., for NASA, under contract NAS5-26555.

## Appendix A
## Choice of the Reduced Speed of Light

We use an RSOL of $\tilde{c}$= 300 km s$^{-1}$ for both the CRs and radiation in our simulations. This makes the simulations computationally feasible by limiting the time-step criterion to $\Delta t \leqslant C_{\rm cour}\Delta x/\tilde{c}$ in all regions of the grid. The choice of $\tilde{c}$ should be irrelevant if it is much faster than the other velocities in the simulation, as the CR propagation equations converge to the same solutions in steady-state independent of $\tilde{c}$. However, the top panel of Figure 11 shows that in many regions during the cloud evolution, the CR streaming velocity is larger than 300 km s$^{-1}$. Consequently, all transport and loss timescales except the advection timescale are slowed down by a factor of $\Gamma_{\rm RSOL} = c/\tilde{c}$= 1000 (Hopkins et al. 2020), which is used to scale the timescales plotted in the bottom panel of Figure 11.

It is not feasible to run the simulations at full resolution with $\tilde{c} \sim 10^3 - 10^4$ km s$^{-1}$ in a reasonable amount of wall clock time. Instead, we test the impact of our choice of $\tilde{c}$ by performing six low-resolution simulations ($N_{\rm gas} = 2 \times 10^5$) that vary the value of $\tilde{c}$. Three of these start with the initial CR background equivalent to that used in the M2e3_E1_D8e25 simulation ($\epsilon_{\rm cr,med} = 1$ eV cm$^{-3}$), and three start with the initial CR energy density used in the M2e3_E10_D8e25 simulation ($\epsilon_{\rm cr,med} = 10$ eV cm$^{-3}$). For each initial CR configuration, we adopt values $\tilde{c}$ = 75, 300, and 1200 km s$^{-1}$. All six tests use the fiducial diffusion coefficient $D_{\parallel} = 8.33 \times 10^{25}$ cm$^2$ s$^{-1}$. The six different runs are listed in Table 4.

Figure 13 shows slice plots of the gas number density (top) and CR energy density (bottom) for the M2e3_E1_D8e25 setup at $t = t_{\rm ff}$ using $\tilde{c}$ = 75 kms$^{-1}$ (left), $\tilde{c}$ = 300 kms$^{-1}$ (middle), and $\tilde{c}$ = 1200 kms$^{-1}$ (right). Increasing $\tilde{c}$ causes faster CR energy losses because the streaming loss timescale $\tau_{\rm str,loss}$ scales inversely with $\tilde{c}$. The biggest discrepancy occurs near the cloud boundaries where streaming energy losses are significant, as discussed in Section 4.1.2. The top left panel of Figure 14 shows the evolution of the median CR energy density as a function of time for various gas densities for the three M2e3_E1_D8e25 setup tests. This plot shows that by $1t_{\rm ff}$ the $\tilde{c}$ = 75 kms$^{-1}$ run has $\epsilon_{\rm cr} \gtrsim 10^{-2}$ eV cm$^{-3}$ in the cloud, while the $\tilde{c}$ = 1200 kms$^{-1}$ run has $\epsilon_{\rm cr} < 10^{-3}$ eV cm$^{-3}$. The variation between different choices of $\tilde{c}$ is slightly more than the factor of 4 difference in $\Gamma_{\rm RSOL}$, which indicates that the choice of $\tilde{c}$ has an impact on the CR energy evolution even greater than the difference expected from timescale analysis.

Another potential consequence of using a low value of $\tilde{c}$ is that CRs can become artificially trapped in dense gas (Hopkins et al. 2020). Since the calculations adopt a Lagrangian frame of reference that moves with the gas, the advection timescale $\tau_{\rm adv}$ is independent of $\tilde{c}$, but the streaming and diffusion timescales $\tau_{\rm str}$ and $\tau_{\rm diff}$ are not. Using a low value of $\tilde{c}$ can cause CR advection to dominate and not allow the CRs to escape through diffusion and streaming. Figure 14 shows that all three tests have slightly elevated values in gas densities $n > 10^4$ cm$^{-3}$ (black lines) at early times but reach a uniform CR energy density in the cloud at slightly earlier times for a higher value of $\tilde{c}$. Still, this difference is minor compared to the discrepancy between the different tests for the same density range, indicating that the enhancement caused by artificial CR trapping is subdominant compared to the differences caused by streaming energy losses. However, this effect may produce more significant differences in the evolution of smaller clouds.

**Table 4**
Simulation Name, RSOL, and Final Values for the SFE for Six Different Tests Varying $\tilde{c}$

| Simulation Name | RSOL [km s$^{-1}$] | SFE (%) |
|---|---|---|
| M2e3_E1_D8e25_RSOL75 | 75 | 9.3 |
| M2e3_E1_D8e25_RSOL300 | 300 | 7.46 |
| M2e3_E1_D8e25_RSOL1200 | 1200 | 7.09 |
| M2e3_E10_D8e25_RSOL75 | 75 | 10.9 |
| M2e3_E10_D8e25_RSOL300 | 300 | 7.8 |
| M2e3_E10_D8e25_RSOL1200 | 1200 | 6.62 |

**Note.** All simulations use $N_{\rm gas} = 2 \times 10^5$ and $D_{\parallel} = 8.33 \times 10^{25}$ cm$^2$ s$^{-1}$.

In addition to these differences in the CR transport, there is a correlation between the value of $\tilde{c}$used and the stellar mass distribution formed. Figure 14 shows that the M2e3_E1_D8e25_RSOL1200 simulation does not have a noticeable increase in the median CR energy density between ∼1.5 and 2.5 $t_{\rm ff}$ like the other M2e3_E1_D8e25 setup tests. The stars formed in that test simulation did not have stellar winds powerful enough to inject a significant amount of CR energy. To illustrate this point, the bottom row of Figure 14 shows a plot of the evolution of the CR energy injected by stellar winds (left) and the most massive star in the simulation (right) for our six test runs. For a given initial CR distribution, a higher value of $\tilde{c}$ produces more rapid initial accretion onto a few massive stars, causing the injected CR energy to rise as the stellar winds become more powerful due to the more massive stars. However, this initial accretion phase is cut off earlier, capping the stellar wind energy. In the M2e3_E1_D8e25_RSOL1200 simulation, no stars form that are massive enough to have stellar winds that noticeably increase the median CR energy density in the cloud.

Despite these caveats, Figure 13 shows that the evolution of the gas density is similar for all choices of $\tilde{c}$. This is partially because the M2e3_E1_D8e25 setup is initialized with $\epsilon_{\rm cr} = 1$ eV cm$^{-3}$, which is not high enough to strongly influence the gas dynamics even with minimal energy losses. Additionally, the effects described on the CRT are not as drastic as they initially seem because at the relevant length scales our choice of $\tilde{c}$ is large enough. Figure 11 shows the timescales for CRs to propagate all the way through the cloud ($L = 3$ pc) through streaming and diffusion *alone* are ≈1–10 Myr, comparable to the advection timescale (which is a good approximation of the dynamical timescale). However, since the advection timescale is independent of $\tilde{c}$, the gas collapse transports CRs through the cloud and helps offset the slow transport timescales. The CR energy density will reach a relatively smooth distribution on smaller timescales than shown in Figure 11 because the simulation resolution is much smaller than the cloud radius ($\Delta x_J \sim 36$ au), and CR gradients at these scales will be wiped out quickly. Figures 2 and 11 show that by 0.5–0.75 $t_{\rm ff}$ the CR

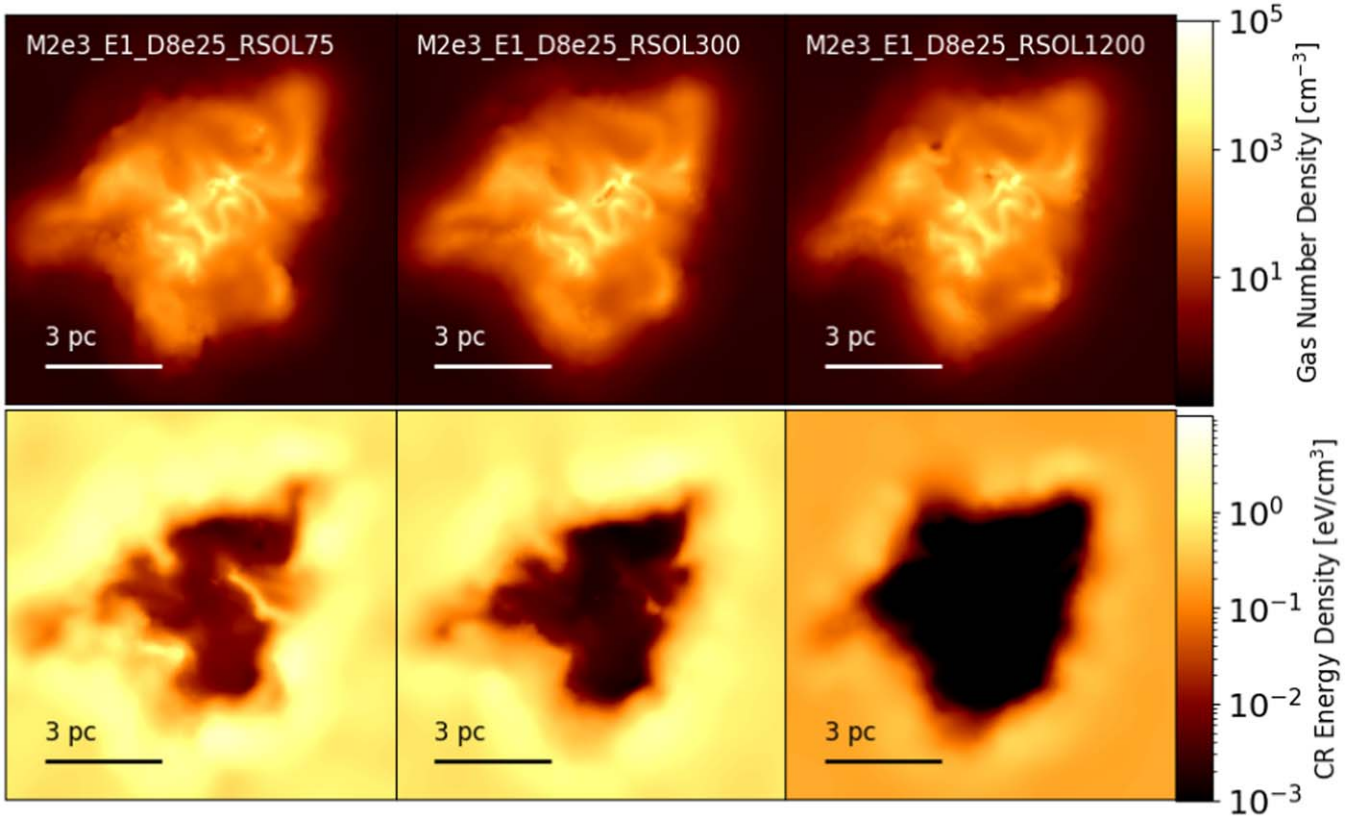


**Figure 13.** Gas number density (top) and CR energy density (bottom) at 1 $t_{\rm ff}$ for the runs with RSOL $\tilde{c} = 75\,{\rm km\,s^{-1}}$ (left), $\tilde{c} = 300\,{\rm km\,s^{-1}}$ (middle), and $\tilde{c} = 1200\,{\rm km\,s^{-1}}$ (right), starting with the M2e3_E1_D8e25 CR distribution.

energy density at $n \gtrsim 500\,{\rm cm^{-3}}$ is roughly independent of gas density, indicating that CRs are indeed able to propagate out of the densest gas.

Furthermore, despite the differences in the stellar accretion, differences in the evolution of the CR distribution in the cloud do not change the SFE until near the end of the cloud evolution. Figure 14, top right, shows the evolution of the SFE for the six different runs. As in Section 3.2, we assume SFE $\approx 7.42 \pm 1.77$ as the $1\sigma$ region, although the exact numbers should not be compared to our main simulations with $N_{\rm gas} = 2 \times 10^6$ as resolution causes variations in the results as well. For both the M2e3_E1_D8e25 variations and M2e3_E10_D8e25 variations, the evolution of the SFE begins similarly for the different values of $\tilde{c}$. However, the time at which star formation slows and the cloud disperses occurs later for a lower choice of $\tilde{c}$, raising the final value of the SFE.

The final values of the SFE for the six runs are shown in Table 4. If we assume SFE $\approx 7.42 \pm 1.77$, then both the M2e3_E1_D8e25_RSOL75 and M2e3_E10_D8e25_RSOL75 tests have values of the SFE above the $1\sigma$ region. The difference between the M2e3_E1_D8e25_RSOL75 and the M2e3_E1_D8e25_RSOL300 tests is $\approx$2%, while between the M2e3_E10_D8e25_RSOL75 and M2e3_E10_D8e25_RSOL300 tests it is $\approx$3%. The RSOL1200 tests did not have as large of a variation in the final SFE from the RSOL300 tests, and only had a difference in the SFE of $\sim$0.35% and $\sim$1.2% for the M2e3_E1_D8e25_RSOL1200 and M2e3_E10_D8e25_RSOL1200 tests, respectively. Since these differences are less than $1\sigma$ and we focus this study on the SFE rather than the IMF, we conclude that using $\tilde{c} = 300\,{\rm km\,s^{-1}}$ is sufficiently resolved for our simulations. However, the trends in the SFE and stellar mass distribution suggest that future numerical simulations of CR propagation in MCs, particularly studies exploring a high-CR environment, should carefully consider the choice of $\tilde{c}$.

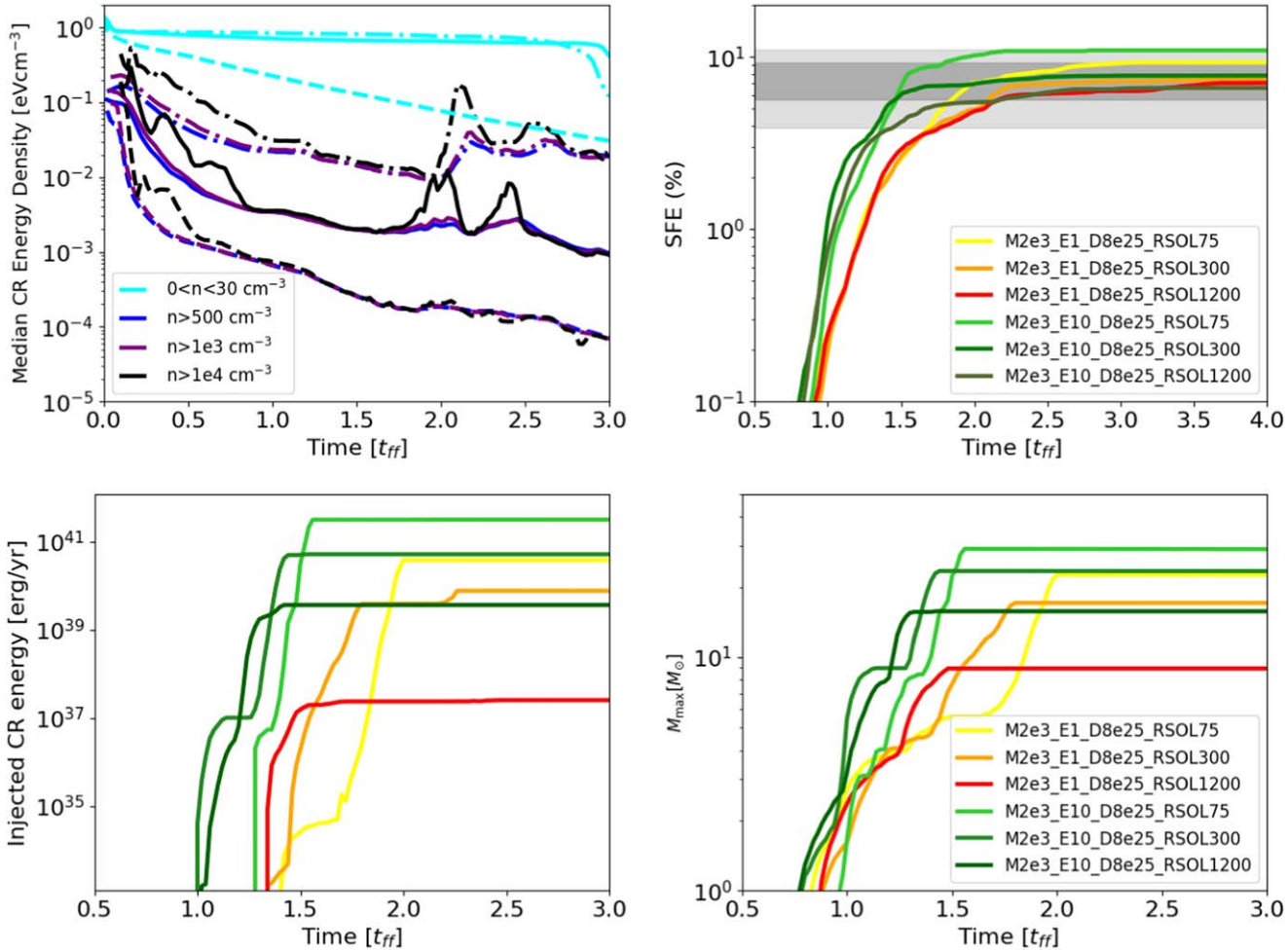


**Figure 14.** Top left: median CR energy density for gas in the indicated density range or lower limit for the M2e3_E1_D8e25_RSOL75 (dashed–dotted), M2e3_E1_D8e25_RSOL300 (solid), and M2e3_E1_D8e25_RSOL1200 (dashed) simulations. Top right: evolution of the SFE for the RSOL tests. Shaded regions are the $1\sigma$ (dark gray) and $2\sigma$ (light gray) final SFE values obtained from a set of 100 $2000M_\odot$ cloud simulations without CRT that vary the initial turbulent seed. We note that both the tests with the fiducial RSOL of $\tilde{c} = 300$ km s$^{-1}$ do not evolve exactly identically to the full-resolution analogs due to numerical differences. Bottom left: evolution of the total CR energy injected by stellar winds for the RSOL tests. Bottom right: evolution of the maximum stellar mass for the RSOL tests.

## Appendix B
## Tests with Varying Physics

Figure 11 shows that for our M2e3_E1_D8e25 simulation, both CR transport and energy losses are dominated by streaming, especially at the cloud boundary. As we discuss in Section 4.1.2, these effects cause CRs that originated in the cloud to lose most of their energy and prevent CRs outside the cloud from propagating in without significant energy losses (Figure 12). In order to confirm these conclusions, we run low-resolution simulations ($N_{\rm gas} = 2 \times 10^5$) out to $\sim 1.5\, t_{\rm ff}$ where we vary the CR transport and loss physics. The first one has identical transport and loss physics to our high-resolution simulations. In the second we disable all heating/cooling interactions with the gas, and consequently all collisional losses (Equations (9) and (10)). In the final test simulation we disable both streaming transport and energy losses (all terms including $v_{\rm st}$ in Equations (4) and (5)). All three of these simulations start with the initial CR background and diffusion coefficient used in the M2e3_E1_D8e25 simulation ($\epsilon_{\rm cr,med}$=1 eV cm$^{-3}$ and $D_\parallel = 8.33 \times 10^{25}$ cm$^2$ s$^{-1}$) and use an RSOL of $\tilde{c} = 300$ km s$^{-1}$. Since these tests are designed as a simple test of the relevant CR physics and losses, we only run them out to $\sim 1.5\, t_{\rm ff}$. The three different runs are listed in Table 5.

**Table 5**
Parameters for Different Tests Varying CR Transport and Loss Physics

| Simulation Name | Heating/Cooling? | Streaming? |
|---|---|---|
| M2e3_E1_D8e25_ALL | Y | Y |
| M2e3_E1_D8e25_NOLOSS | N | Y |
| M2e3_E1_D8e25_NOST | Y | N |

**Note.** All simulations use $N_{\rm gas} = 2 \times 10^5$, $\epsilon_{\rm cr,med} = 1$ eV cm$^{-3}$, and $D_\parallel = 8.33 \times 10^{25}$ cm$^2$ s$^{-1}$.

Figure 15 shows slice plots of the gas number density (top) and CR energy density (bottom) of the three different simulations at $t = t_{\rm ff}$. Both the gas number density and CR energy density appear almost identical for the M2e3_E1_D8e25_ALL (left) and M2e3_E1_D8e25_NOLOSS (middle) simulations. Figure 16 shows the time evolution of the CR energy density for the three different simulations. The evolution of the median CR energy density is indistinguishable for the M2e3_E1_D8e25_ALL (solid) and M2e3_E1_D8e25_NOLOSS (dashed) simulations. These results confirm our conclusion that

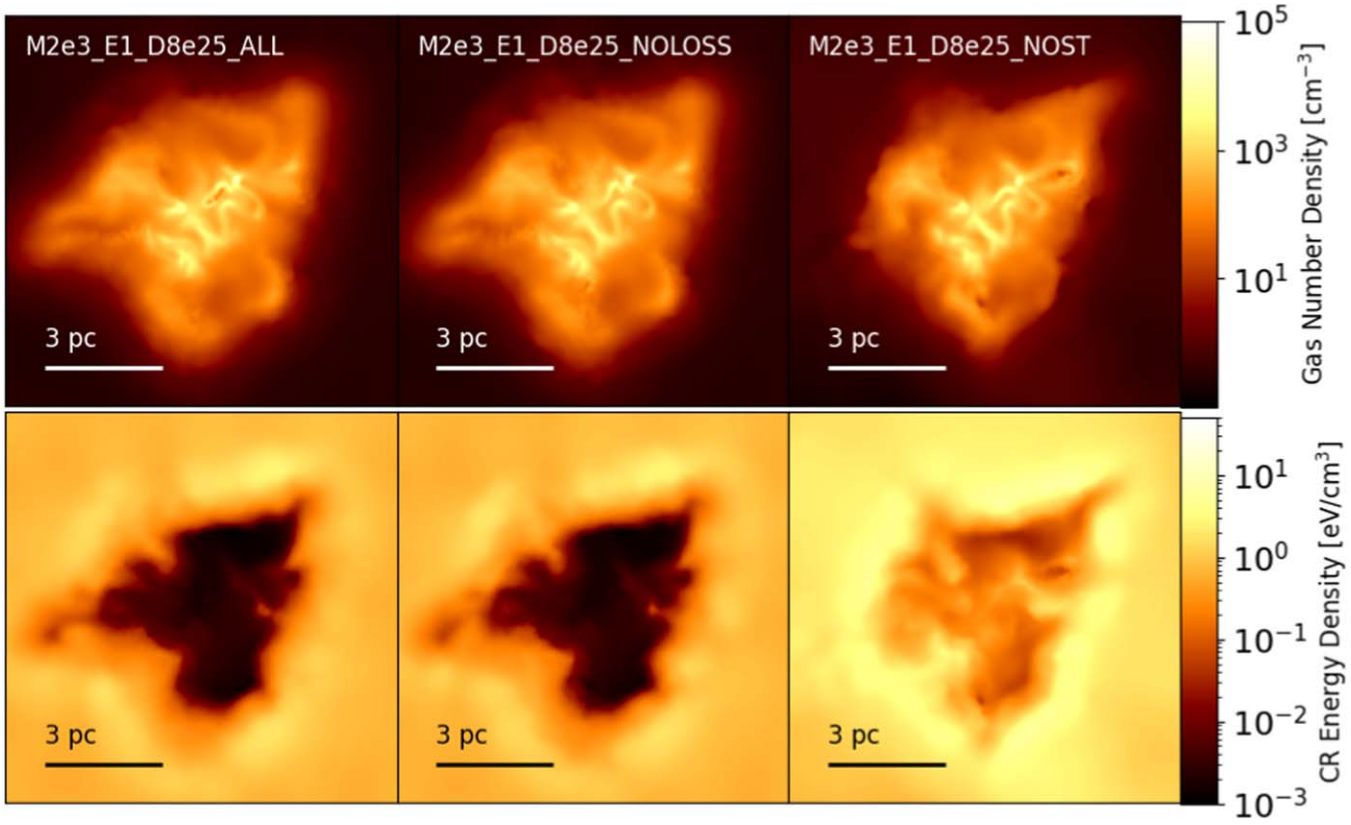


**Figure 15.** Gas number density (top) and CR energy density (bottom) at $1t_{\rm ff}$ for simulations comparing our M2e3_E1_D8e25 setup (left) to a setup with no collisional losses (middle) and a setup with no streaming transport and energy losses (right).

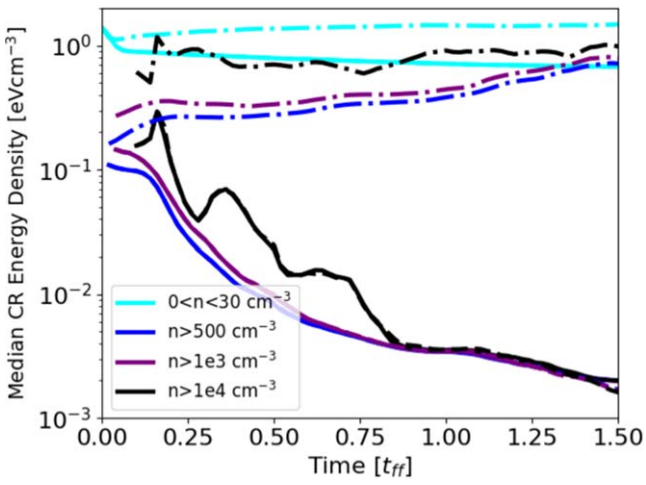


**Figure 16.** Median CR energy density for gas in the indicated density range or lower limit for the M2e3_E1_D8e25_ALL (solid) and M2e3_E1_D8e25_NO-LOSS (dashed) and M2e3_E1_D8e25_NOST (dashed–dotted) simulations.

CR collisional losses are insignificant compared to streaming energy losses in our simulations.

In contrast, our simulation with no streaming transport or losses shows significant differences. The right column of Figure 15 shows that the gas density for the M2e3_E1_D8e25_NOST simulation appears similar to the other two simulations at $t = t_{\rm ff}$ but not indistinguishable. However, the CR energy density (bottom) is much higher than in the other two simulations. This is especially true in the cloud and at the cloud boundary, where it is up to 2 orders of magnitude higher. Although there is still a slight enhancement in the CR energy density at the cloud boundary due to magnetic field effects (Section 4.1.2), CRs no longer lose energy in this region and can propagate through into the cloud. Figure 16 shows that the median CR energy density for this simulation (dashed–dotted) rises at all gas densities inside the cloud. The CRs are advected with the gas as the cloud collapses, leading to the enhancement at higher densities. Finally, the slight increase in the CR energy density outside the cloud (cyan) is due to diffusive reacceleration, allowing the CRs to gain energy as they propagate.

## ORCID iDs

Margot Fitz Axen https://orcid.org/0000-0001-7220-5193
Stella Offner https://orcid.org/0000-0003-1252-9916
Philip F. Hopkins https://orcid.org/0000-0003-3729-1684
Mark R. Krumholz https://orcid.org/0000-0003-3893-854X
Michael Y. Grudić https://orcid.org/0000-0002-1655-5604

## References

Ackermann, M., Ajello, M., Allafort, A., et al. 2011, Sci, 334, 1103
Aharonian, F., Yang, R., & de Oña Wilhelmi, E. 2019, NatAs, 3, 561
Aharonian, F. A. 2013, APh, 43, 71
Bate, M. R., & Keto, E. R. 2015, MNRAS, 449, 2643
Behrens, E., Mangum, J. G., Holdship, J., et al. 2022, ApJ, 939, 119
Bertoldi, F., & McKee, C. F. 1992, ApJ, 395, 140
Bialy, S., Belli, S., & Padovani, M. 2022, A&A, 658, L13
Blasi, P. 2013, A&ARv, 21, 70
Booth, C. M., Agertz, O., Kravtsov, A. V., & Gnedin, N. Y. 2013, ApJL, 777, L16
Bustard, C., & Zweibel, E. G. 2021, ApJ, 913, 106
Butsky, I. S., & Quinn, T. R. 2018, ApJ, 868, 108
Bykov, A. M., Marcowith, A., Amato, E., et al. 2020, SSRv, 216, 42
Cabedo, V., Maury, A., Girart, J. M., et al. 2023, A&A, 669, A90

Caselli, P., Walmsley, C. M., Terzieva, R., & Herbst, E. 1998, ApJ, 499, 234
Ceccarelli, C., Dominik, C., López-Sepulcre, A., et al. 2014, ApJL, 790, L1
Ceccarelli, C., Hily-Blant, P., Montmerle, T., et al. 2011, ApJL, 740, L4
Cesarsky, C. J., & Volk, H. J. 1978, A&A, 70, 367
Chabrier, G. 2005, in The Initial Mass Function 50 Years Later, ed. E. Corbelli, F. Palla, & H. Zinnecker, Vol. 327 (Berlin: Springer), 41
Chan, T. K., Kereš, D., Hopkins, P. F., et al. 2019, MNRAS, 488, 3716
Chandran, B. D. G. 2000, ApJ, 529, 513
Commerçon, B., Marcowith, A., & Dubois, Y. 2019, A&A, 622, A143
Cummings, A. C., Stone, E. C., Heikkila, B. C., et al. 2016, ApJ, 831, 18
Cunningham, A. J., Klein, R. I., Krumholz, M. R., & McKee, C. F. 2011, ApJ, 740, 107
Dalgarno, A. 2006, PNAS, 103, 12269
Dashyan, G., & Dubois, Y. 2020, A&A, 638, A123
Ensslin, T. A., Biermann, P. L., Kronberg, P. P., & Wu, X.-P. 1997, ApJ, 477, 560
Everett, J. E., & Zweibel, E. G. 2011, ApJ, 739, 60
Evoli, C., Aloisio, R., & Blasi, P. 2019, PhRvD, 99, 103023
Farber, R., Ruszkowski, M., Yang, H. Y. K., & Zweibel, E. G. 2018, ApJ, 856, 112
Farcy, M., Rosdahl, J., Dubois, Y., Blaizot, J., & Martin-Alvarez, S. 2022, MNRAS, 513, 5000
Fatuzzo, M., & Adams, F. C. 2014, ApJ, 787, 26
Federrath, C., & Klessen, R. S. 2012, ApJ, 761, 156
Ferrière, K. M. 2001, RvMP, 73, 1031
Fiedler, R. A., & Mouschovias, T. C. 1993, ApJ, 415, 680
Fitz Axen, M., Offner, S. S. S., Gaches, B. A. L., et al. 2021, ApJ, 915, 43
Fontani, F., Ceccarelli, C., Favre, C., et al. 2017, A&A, 605, A57
Gaches, B. A. L., & Offner, S. S. R. 2018, ApJ, 861, 87
Gatto, A., Walch, S., Naab, T., et al. 2017, MNRAS, 466, 1903
Girichidis, P., Pfrommer, C., Pakmor, R., & Springel, V. 2022, MNRAS, 510, 3917
Girichidis, P., Werhahn, M., Pfrommer, C., Pakmor, R., & Springel, V. 2024, MNRAS, 527, 10897
Girichidis, P., Naab, T., Walch, S., et al. 2016, ApJL, 816, L19
Glover, S. C. O., & Clark, P. C. 2012, MNRAS, 426, 377
Goto, M. 2014, in IAU Symp.303, The Galactic Center: Feeding and Feedback in a Normal Galactic, ed. L. O. Sjouwerman, C. C. Lang, & J. Ott (Cambridge: Cambridge Univ. Press), 429
Grudić, M. Y., Guszejnov, D., Hopkins, P. F., Offner, S. S. R., & Faucher-Giguère, C.-A. 2021, MNRAS, 506, 2199
Grudić, M. Y., Guszejnov, D., Offner, S. S. R., et al. 2022, MNRAS, 512, 216
Grudić, M. Y., Offner, S. S. R., Guszejnov, D., Faucher-Giguère, C.-A., & Hopkins, P. F. 2023, OJAp, 6, 48
Guo, F., & Oh, S. P. 2008, MNRAS, 384, 251
Guszejnov, D., Grudić, M. Y., Hopkins, P. F., Offner, S. S. R., & Faucher-Giguère, C.-A. 2021, MNRAS, 502, 3646
Guszejnov, D., Grudić, M. Y., Offner, S. S. R., et al. 2022, MNRAS, 515, 4929
Habegger, R., Zweibel, E. G., & Wong, S. 2023, ApJ, 951, 99
Hanasz, M., Lesch, H., Naab, T., et al. 2013, ApJL, 777, L38
Hennebelle, P., & Chabrier, G. 2008, ApJ, 684, 395
Holdship, J., Mangum, J. G., Viti, S., et al. 2022, ApJ, 931, 89
Holguin, F., Ruszkowski, M., Lazarian, A., Farber, R., & Yang, H. Y. K. 2019, MNRAS, 490, 1271
Hopkins, P. F. 2012, MNRAS, 423, 2037
Hopkins, P. F. 2015, MNRAS, 450, 53
Hopkins, P. F. 2016, MNRAS, 462, 576
Hopkins, P. F., Butsky, I. S., Panopoulou, G. V., et al. 2022a, MNRAS, 516, 3470
Hopkins, P. F., Chan, T. K., Ji, S., et al. 2021a, MNRAS, 501, 3640
Hopkins, P. F., Chan, T. K., Squire, J., et al. 2021b, MNRAS, 501, 3663
Hopkins, P. F., & Raives, M. J. 2016, MNRAS, 455, 51
Hopkins, P. F., Squire, J., & Butsky, I. S. 2022b, MNRAS, 509, 3779
Hopkins, P. F., Squire, J., Butsky, I. S., & Ji, S. 2022c, MNRAS, 517, 5413
Hopkins, P. F., Squire, J., Chan, T. K., et al. 2021c, MNRAS, 501, 4184
Hopkins, P. F., Wetzel, A., Kereš, D., et al. 2018, MNRAS, 477, 1578
Hopkins, P. F., Chan, T. K., Garrison-Kimmel, S., et al. 2020, MNRAS, 492, 3465
Hopkins, P. F., Wetzel, A., Wheeler, C., et al. 2023, MNRAS, 519, 3154
Indriolo, N., & McCall, B. J. 2012, ApJ, 745, 91
Indriolo, N., Neufeld, D. A., Gerin, M., et al. 2015, ApJ, 800, 40
Jacob, S., Pakmor, R., Simpson, C. M., Springel, V., & Pfrommer, C. 2018, MNRAS, 475, 570
Ji, S., Chan, T. K., Hummels, C. B., et al. 2020, MNRAS, 496, 4221
Jiang, Y.-F., & Oh, S. P. 2018, ApJ, 854, 5
Jubelgas, M., Springel, V., Enßlin, T., & Pfrommer, C. 2008, A&A, 481, 33
Kálosi, Á., Gamer, L., Grieser, M., et al. 2023, ApJL, 955, L26
Krumholz, M. R., Crocker, R. M., & Offner, S. S. R. 2023, MNRAS, 520, 5126
Krumholz, M. R., Crocker, R. M., Xu, S., et al. 2020, MNRAS, 493, 2817
Kuffmeier, M., Zhao, B., & Caselli, P. 2020, A&A, 639, A86
Kulsrud, R., & Pearce, W. P. 1969, ApJ, 156, 445
Kulsrud, R. M. 2005, Plasma Physics for Astrophysics (Princeton, NJ: Princeton Univ. Press)
Lamers, H. J. G. L. M., Snow, T. P., & Lindholm, D. M. 1995, ApJ, 455, 269
Lee, A. T., Offner, S. S. R., Kratter, K. M., Smullen, R. A., & Li, P. S. 2019, ApJ, 887, 232
Levermore, C. D. 1984, JQSRT, 31, 149
Li, P. S., McKee, C. F., & Klein, R. I. 2015, HiA, 16, 386
Liu, B., Yang, R.-z., & Chen, Z. 2022, MNRAS, 513, 4747
Maud, L. T., Moore, T. J. T., Lumsden, S. L., et al. 2015, MNRAS, 453, 645
McKee, C. F., & Ostriker, E. C. 2007, ARA&A, 45, 565
Mouschovias, T. C., & Spitzer, L. J. 1976, ApJ, 210, 326
Neufeld, D. A., & Wolfire, M. G. 2017, ApJ, 845, 163
Offner, S. S. R., Klein, R. I., McKee, C. F., & Krumholz, M. R. 2009, ApJ, 703, 131
Offner, S. S. R., Moe, M., Kratter, K. M., et al. 2023, in ASP Conf. Ser. 534, Protostars and Planets VII, ed. S. Inutsuka et al. (San Francisco, CA: ASP), 275
Padoan, P., & Nordlund, Å. 2011, ApJL, 741, L22
Padoan, P., & Scalo, J. 2005, ApJL, 624, L97
Padovani, M. 2023, Physics and Chemistry of Star Formation: The Dynamical ISM Across Time and Spatial Scales. Proc. of the 7th Chile-Cologne-Bonn Symp., ed. V. Ossenkopf-Okada et al. (Cologne: Univ. Cologne), 237
Padovani, M., & Galli, D. 2011, A&A, 530, A109
Padovani, M., Galli, D., & Glassgold, A. E. 2009, A&A, 501, 619
Padovani, M., Galli, D., Hennebelle, P., Commerçon, B., & Joos, M. 2014, A&A, 571, A33
Padovani, M., Hennebelle, P., & Galli, D. 2013, A&A, 560, A114
Padovani, M., Marcowith, A., Hennebelle, P., & Ferrière, K. 2016, A&A, 590, A8
Padovani, M., Ivlev, A. V., Galli, D., et al. 2020, SSRv, 216, 29
Pakmor, R., Pfrommer, C., Simpson, C. M., & Springel, V. 2016, ApJL, 824, L30
Pandey, P., Lopez, L. A., Rosen, A. L., et al. 2024, arXiv:2404.19001
Parizot, E., Marcowith, A., van der Swaluw, E., Bykov, A. M., & Tatischeff, V. 2004, A&A, 424, 747
Pineda, J. E., Sipilä, O., Segura-Cox, D. M., et al. 2024, A&A, 686, A162
Rivilla, V. M., García De La Concepción, J., Jiménez-Serra, I., et al. 2022, FrASS, 9, 829288
Rosen, A. L., & Krumholz, M. R. 2020, AJ, 160, 78
Rosen, A. L., Offner, S. S. R., Foley, M. M., & Lopez, L. A. 2021, arXiv:2107.12397
Sabatini, G., Bovino, S., & Redaelli, E. 2023, ApJL, 947, L18
Sabatini, G., Bovino, S., Giannetti, A., et al. 2020, A&A, 644, A34
Salem, M., Bryan, G. L., & Hummels, C. 2014, ApJL, 797, L18
Sampson, M. L., Beattie, J. R., Krumholz, M. R., et al. 2023, MNRAS, 519, 1503
Semenov, V. A., Kravtsov, A. V., & Caprioli, D. 2021, ApJ, 910, 126
Shingledecker, C. N., Bergner, J. B., Le Gal, R., et al. 2016, ApJ, 830, 151
Silsbee, K., Ivlev, A. V., Padovani, M., & Caselli, P. 2018, ApJ, 863, 188
Simpson, C. M., Pakmor, R., Marinacci, F., et al. 2016, ApJL, 827, L29
Skilling, J. 1975, MNRAS, 172, 557
Skilling, J., & Strong, A. W. 1976, A&A, 53, 253
Skinner, M. A., & Ostriker, E. C. 2013, ApJS, 206, 21
Smith, N. 2014, ARA&A, 52, 487
Smith, R. J., Treß, R. G., Sormani, M. C., et al. 2020, MNRAS, 492, 1594
Squire, J., Hopkins, P. F., Quataert, E., & Kempski, P. 2021, MNRAS, 502, 2630
Stone, E. C., Cummings, A. C., Heikkila, B. C., & Lal, N. 2019, NatAs, 3, 1013
Sun, X.-N., Yang, R.-Z., Liang, Y.-F., et al. 2020, A&A, 639, A80
Thomas, T., Pfrommer, C., & Pakmor, R. 2023, MNRAS, 521, 3023
Trotta, R., Jóhannesson, G., Moskalenko, I. V., et al. 2011, ApJ, 729, 106
Uhlig, M., Pfrommer, C., Sharma, M., et al. 2012, MNRAS, 423, 2374
Vaupré, S., Hily-Blant, P., Ceccarelli, C., et al. 2014, A&A, 568, A50
Vink, J. 2012, A&ARv, 20, 49
Völk, H. J., Aharonian, F. A., & Breitschwerdt, D. 1996, SSRv, 75, 279
Wentzel, D. G. 1971, ApJ, 163, 503
Wiener, J., Pfrommer, C., & Oh, S. P. 2017, MNRAS, 467, 906

Williams, J. P., Bergin, E. A., Caselli, P., Myers, P. C., & Plume, R. 1998, ApJ, 503, 689
Wurster, J., Bate, M. R., & Price, D. J. 2018, MNRAS, 480, 4434
Xu, S., & Lazarian, A. 2017, NJPh, 19, 065005
Yang, R.-z., & Aharonian, F. 2017, A&A, 600, A107
Yang, R.-z., de Oña Wilhelmi, E., & Aharonian, F. 2018, A&A, 611, A77
Zweibel, E. G. 2013, PhPl, 20, 055501
Zweibel, E. G. 2017, PhPl, 24, 055402